A Study of Low Frequency Vibration Isolation System for Large Scale Gravitational Wave Detectors

Department of Physics, Graduate School of Science
University of Tokyo

Takanori Sekiguchi

January 2016

Abstract

Gravitational waves are distortions of spacetime which propagate through space at the speed of light. Several large-scale interferometric gravitational wave detectors have been constructed for their direct detection. So-called first generation detectors (TAMA, GEO, LIGO, Virgo) have performed scientific observations. However, they had a detection probability of only a few percent per year at best and gravitational waves have not been detected by them yet. More sensitive detectors which are capable of detecting many events per year are necessary. Based on the experience gathered with the first generation detectors, second generation detectors have been designed with thousands of times higher probability of gravitational wave detection. A Japanese second generation detector, LCGT (Large-scale Cryogenic Gravitational wave Telescope), was funded recently and is now being constructed.

Seismic motion is an inevitable noise source for ground-based interferometric gravitational wave detectors. The continuous and random motion of the ground can excite the motions of the optical components of an interferometer, resulting in a displacement noise (*seismic noise*). In order to reduce the noise, vibration isolation systems are installed to isolate the optics in the interferometer from ground. The vibration isolation systems for LCGT will be based on the Seismic Attenuation System (SAS), which has been developed for TAMA and advanced LIGO. The objective of the system is to achieve seismic attenuation starting from sufficiently low frequencies ($\lesssim 0.1Hz$) and to reduce the Root Mean Square (RMS) displacement and velocity of the optics below the level of ~ 0.1 μm and 0.1 μm/s, for stable operation and fast lock acquisition of the interferometer.

One needs to construct mechanical models of vibration isolation systems, to estimate their attenuation performance and to design them. For these purposes, I have developed three-dimensional rigid-body models of the vibration isolation systems for LCGT, in which the system is assumed to be a group of rigid-bodies with 6 degrees of freedom (DoFs) for each. The rough estimation of the attenuation performance can be achieved by the use of simple point-mass models, in which the system is regarded as a combination of point masses and ideal springs connecting with them. However, they are uni-dimensional in principle and therefore they cannot take into account the cross-talks between other DoFs. The rigid-body models can take into account these cross-couplings and treat the rotational motions of the suspended objects. By the use of the rigid-body models, I have estimated the attenuation performance of the vibration isolation systems for LCGT in both translational

and rotational DoFs, and performed considerations that affected and improved the SAS design.

Table of Contents

Gravitational waves

Chapter 1

1.1 Theory and background

Laser interferometer for gravitational wave detection

Chapter 2

2.1 Theory and background

Vibration Isolation

Chapter 3

3.1 Seismic Noise

Static seismic vibration is one of the primary and unavoidable noise sources in ground-based gravitational wave detectors. Vibration of the ground surface where an interferometer stands transmits to the suspended mirrors and produce the differential displacement, which mimics the signals from gravitational waves.

Seismic vibration is excited by natural phenomena like oceanic and atomospheric activities and also by artifical activities like city traffics. Therefore the magnitude of static seismic vibration varies by time and place, depending on surrounding environment such as weather condition and traffic activities. It is known that the seismic vibration decreases significantly in underground environment, since the surrounding rocks isolate the vibration from atmospheric and human activities on ground surface. This is one of the biggest motivations to build gravitational wave detecotrs underground althgough there are difficulties like construction costs and safety issues.

The optics

3.2 Seismic Vibration Spectrum

Seismic Attenuation System

Chapter 4

Various vibration isolation systems invented for different gravitational wave detectors were introduced in the previous chapter. In this chapter, I focus attention on vibration isolation system for the main optics in the KAGRA interferometer, often called Seismic Attenuation System (SAS).

Active suspension controls

Chapter 5

5.1 Motivation of active controls

Mechanics of suspension systems are designed so that they achieve sufficient vibration isolation in the frequency band of gravitational wave observation. On the other hand, the suspension systems also have to suppress the mirror vibration outside the band, for stable operation of the interferometer. Without any damping mechanisms, mirror vibration tends to be enhanced at low frequencies by mechanical resonces which typically possess high quality factors. Also, low frequency oscillators often suffer from thermal drifts or mechanical creeps, which blow the suspended mirrors away from the controllable range during the interferometer operation.

In order to suppress the low frequency vibration due to these mechanical characteristics, we control the vibration of mechanical components by the use of vibration sensors and actuators. Note that damping of mechanical resonances can be also achieved by passive dampers such as eddy-current dampers. Passive dampers are stable and easy of maintainance once they are installed to the suspension systems. Active control systems are rather delicate and we have to design the control servo carefully to operate them stably. On the other hand, active systems are more flexible and can be switched easily after installed to the suspension systems. We often need the flexiblity since different controls are required depending on the states of the interferometer and surrounding environment such as temperature and seismic vibration levels. This becomes a big motivation of using active control systems regardless of the complexity.

Another point we have to take care regarding active control systems is the control noise. Noises can be introduced by electronics of vibration sensors and actuators, and also by servos such as quantization errors in digital control systems. We have to make sure that the control noises do not contaminate the interferometer sensitivity any more than the required level.

5.2 Requirement on active controls

5.2.1 Interferometer phases and requirements

As mentioned in the previous section. there are different requirements on the active controls depending on the operation status of the interferometer. Here the operation status of the interferometer are categorized into three phases: the calm down phase, lock acquisition phase, and observation phase.

In the calm down phase, the suspension systems are under large disturbances and the mirrors are swinging in large amplitudes. In this phase, signals for some delicate sensors and week actuators for the active controls can saturate due to the large oscillation amplitude. One has to calm down the vibration using sensors and actuators with sufficient range, and set the position or orientation of masses back to the nominal places. Active controls in this phase require robustness rather than quietness. The fast we get back the suspension systems into working status, the more observation time we can acquire for gravitational wave observation. Thus decay times of the mechanical reosnances should be minimized in this phase for fast recovery.

In the lock acquisition phase, the mirrors in the interferometer are brought to their operation points to get ready for gravtitaional wave observation. For smooth lock acquisition of the interferometer, velocities of the mirrors have to be suppressed so that control forces can freeze their motion and trap them into the linear regime of the interferometer signals. Thence the active controls in this phase are required to minimize the velocities of the suspended mirrors. Typically the RMS velocities of the suspended mirrors have to be suppressed less than 1 μm/sec for smooth lock acquisition of optical cavities. Note that the RMS velocity of the ground vibration is roughly 1 μm/sec and the RMS velocities of the suspended mirrors tend to be enhanced by mechanical resonances with high Q factors. Damping controls for mechanical resonances are demanded, while we have to take care of control noises since they might enhance mirror velocities. The requirements on mirror velocities are discussed in details later.

After the lock acquisition achieved successfully, we get into the observation phase in which the interferometer is under operation and gravitational wave observation is taken in place. In this phase, silent controls are required so that the control noises do not contaminate the detector sensitivity in the observation frequency band (> 10 Hz). Some noisy control loops should be opened or their control gains should be reduced. While at the same time the mirror displacements and orientation have to be kept in a certain range so that the interferometer is kept with good sensitivity to gravitational waves.

The phases of interferometer consitions and requirements on the active controls are summarized in Fig. 5.1.

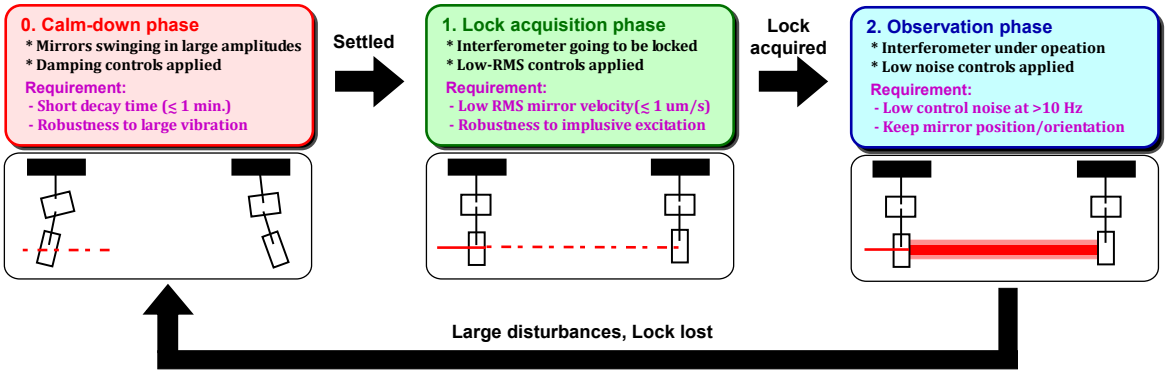

Figure 5.1: Digram of active control phases and the requirements in each phase.

5.2.2 Mirror velocity requirement

As discussed in section **??**, control signals of a linear optical cavity and a Michelson interferometer can be obtained by using frontal modulation technique. By demodulating detected laser power in a proper phase, one can obtain a control signal proportional to the optical cavity length around the operation point. The linear range of the control signal can be roughly calculated from the finesse of the cavity ($\mathcal{F}$) and wave length of the laser light (λ) as

$$\Delta L_{\rm lin} = \frac{\lambda}{2\mathcal{F}}. \tag{5.1}$$

The finesses of the cavities are 38 for the signal recycling cavity, 57 for the power recycling cavity and 1550 for the arm cavities (and 1 for the Michelson interferometer) in the KAGRA interferometer. For the arm cavities, we plan to use green lock scheme and the finesse for the green laser will be set ~ 50.

In order to acquire the lock of an optical cavity, the velocity of cavity length change should be nulled by feedback forces applied to suspended mirrors while the mirrors pass through the linear range. The maximum momentum applied to the suspended mirror by feedback force is limited by staying time of mirrors in the linear regime, the control bandwidth and maximum actuation power of coils.

When the control bandwidth is not large enough, the servo responds too slowly and fails to apply sufficient feedback force before the mirrors pass by the linear regime. The control bandwidth would be limited by response of actuators and existence of mechanical resonances. For the lock acquisition of the arm cavities, we can use voltage controlled oscillators (VCOs) to modulate the laser frequencies as actuators, which have large controllable range and bandwidth. These actuators are free from mechanical resonances of mirrors and therefore we can set the control bandwidth as high as 10 kHz. On the otherhand, lock acquisition about the other DoFs should be accomplished by mechanical actuators attached on mirrors and the bandwidth is limited by existence of mechanical resonances especially

from violin modes of suspension wires which produce peaks in the frequency response around 200 Hz and its harmonics. Thence we need to set the control bandwidth as low as 50 Hz for these DoFs.

Assuming that the actuators have sufficient actuation range and feedback controls are applied only during the time mirrors are in the linear regime, the requirement on the incident velocity of the cavity length change to acquire the lock is calculated as

$$v_{\rm in} \lesssim \omega_b \Delta L_{\rm lin} = \frac{\omega_b \lambda}{2\mathcal{F}}. \tag{5.2}$$

Here ω_b is the control bandwidth or unity gain frequency of the feedback loop. Note that actual feedback signals are non-linear to the cavity length and the requirement could differ if the non-linearity is taken into account, but the order should be the same.

In actual cases, maximum forces which can be applied by the actuators are limited from the point of view of control noise requirement. The stronger actuators we use, the more noise introduced to the mirror displacement in the observation frequency band. Typically the voltage applied on the coil magnet actuators has a noise level $\tilde{V}_{\rm n} \sim 10^{-8}$ $\mu{\rm V}/\sqrt{\rm Hz}$ around 10 Hz and the maximum applicable voltage is $V_{\rm max}$ =10 V. The coil driving noise should be suppresed lower than the required displacement noise of the mirrors. Thence maximum acceleration applicable on the mirror is calculated as

$$a_{\rm max} = \frac{V_{\rm max}}{\tilde{V}_n} \tilde{x}_{\rm req} \omega_{\rm obs}^2. \tag{5.3}$$

Here $\tilde{x}_{\rm req}$ is the required displacement noise level (in ${\rm m}/\sqrt{\rm Hz}$) and $\omega_{\rm obs}$ is the frequency at which the noise requirement should be satisfied. In our case, the requirement gets strictest at $f_{\rm obs} = 10$ Hz.

Here we set different assumption that the control bandwidth is large enough but the actuators can apply limited acceleration ($a_{\rm max}$) on the mirrors. The requirement on the velocity to achieve lock acquisition during the mirrors stay in the linear regime is calculated as

$$v_{\rm in} \lesssim \sqrt{2 a_{\rm max} \Delta L_{\rm lin}}. \tag{5.4}$$

Cavity/interferometer	Requirement from BW	Requirement from $a_{\rm max}$
Arm cavities	10	–
Power recycling cavity	2.8	37
Signal recycling cavity	4.1	3.2
Michelson interferometer	157	20

Table 5.1: Requirement

5.3 Active Controls for KAGRA-SAS

As described in the previous chapter, SAS has a feature of utilizing low frequency oscillators such as inverted pendulums and GAS filters. Such oscillators often suffer from large thermal drift and creep due to cracks inside elastic components. Therefore active DC controls are required to hold the oscillators back to their nominal positions. Regarding the controls for high frequencies, active damping controls are required to suppress the vibration due to mechanical resonances of the suspension systems.

The follwing figure shows the schematics of active control loops for KAGRA-SAS. The top stage held by inverted pendulums is controlled by the use of two kinds of sensors: displacement sensors and seismeters. The displacement sensors measure the relative displacement between the top stage and the frame fixed to the ground. They are used to compensate the drift of the inverted pendulums. Seismometers, or accelerometers measure the vibration of the top stage with respect to the inertial frame. They are used to damp the pendulum modes of the masses suspended below.

Each GAS filter possesses a displacement sensor on the vertical axis to measures the displacement of the keystone with respect to the frame holding the springs. Signals from the displacement sensor are used to compensate the drift of the springs and to damp the resonances.

The vibration of the payload is observed by the use of displacement sensors which measure the relative displacements of the intermediate mass and mirror with respect to their recoil masses. They are used to damp mechanical resonances of the payload which cannot be damped by the top stage active control. Especially, tilt motions of the mirror can be only controlled in this part since the intermediate mass is suspended by a single wire and the tilt motions are seperated from the tilt of upper masses.

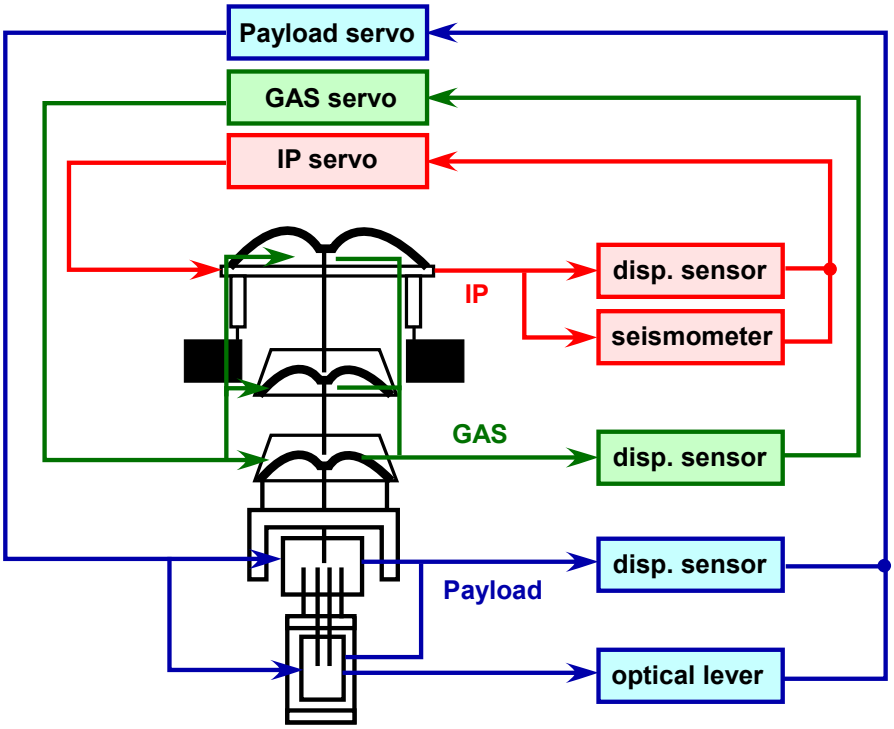

Figure 5.2: Schematics of the active control structure for KAGRA-SAS.

Performance test on individual SAS components

Chapter 6

6.1 Overview

6.2 倒立振り子の制御

6.2.1 制御試験の目的

6.2.2 実験セットアップ

倒立振り子の制御実験のセットアップを図 6.1 に示す。倒立振り子によって支えられたトップステージには鉛直方向防振用の GAS フィルターが搭載され、GAS フィルターよりワイヤーにてマスが懸架される。懸架されるマスの質量は GAS フィルターが支える重量に等しく約 330 kg である。倒立振り子の共振周波数は 100-120 mHz に調整されている。トップステージの水平面内の動きは LVDT，geophone の 2 種類のセンサーを用いて測定され、LVDT は地面に対するステージの変位を、geophone は慣性系に対するステージの速度を測定する。センサーの信号は ADC (Analog to Digital Converter) を通じてデジタルシステムに送られ、デジタルシステム内で処理された信号が DAC (Digital to Analog Converter) を通じてコイル-磁石アクチュエータに向かいトップステージの動きを制御する。

トップステージ上のセンサーおよびアクチュエータの配置を図 6.1 に示す。ステージの 3 自由度の動きを測定するため、制御に用いる LVDT および geophone がそれぞれ 3 個ずつ 120 度離れた位置に配置されている。トップステージを駆動するためのコイル-磁石アクチュエータは LVDT と同軸上に配置されている。またセンサーやアクチュエータの雑音といった制御雑音の影響を調べるため、制御ループ外センサーとしてステージの X 軸方向の並進モードを見る geophone をステージ上に配置した。

ステージの DC 位置を調整するため、ステッピングモーターで駆動するばねが 3 箇所に配置されている。DC 位置調整用のばねの構造を図 6.3 に示す。ステッピングモータでスライドするブロックには厚さ 0.3 mm の 48Si7 鉄の板ばねが 2 枚取り付けられ、ブロックが移動すると左右のばねの引張力が変化しブロックが移動した向きにトップステージが引

Figure 6.1: 倒立振り子の制御実験のセットアップ

Figure 6.2: トップステージ上のセンサーおよびアクチュエータの配置

き寄せられる。板ばねにより生じる復元力は倒立振り子自身が持つ復元力よりも小さく倒立振り子の動作に大きな影響を与えないようになっている。

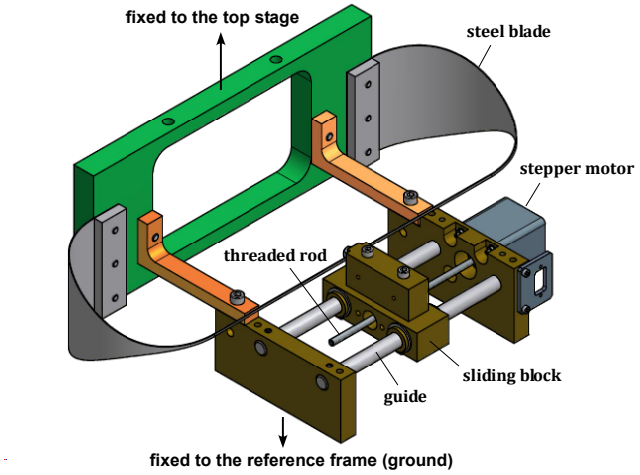

Figure 6.3: トップステージの DC 位置調整用のばね＋スライダー機構

倒立振り子の制御ダイアグラムを図 6.4 に示す。センサー (LVDT，geophone) の信号はキャリブレーション結果や周波数応答の補正により変位情報に変換された後、座標変換によりステージの x, y, θ 座標の変位に変換される。座標変換は 3×3 の変換行列 S によって行われる。2 種類のセンサーで測定された各座標の変位はそれぞれサーボフィルターを通り、足し合されて各座標に関するアクチュエータの信号となる。各座標に関するアクチュエータの制御信号は、座標変換（3×3 変換行列 D）によりステージ上に配置された各アクチュエータに対する信号に変換され、ステージの動きが制御される。

Figure 6.4: 倒立振り子の制御ダイアグラム

6.2.3 センサーの準備と雑音評価

LVDT

LVDT は地面に対するトップステージの相対変位を測定し、主にステージの DC 制御に用いられる。LVDT はコイル-磁石アクチュエータと一体になっており、図 6.5 に示されるような構造をしている。変調磁場を発生させる emitter coil はトップステージ側に固定され、変調磁場による誘導起電力を受ける receiver coils は地面側に固定される。

Figure 6.5: LVDT とコイル磁石アクチュエータのユニット

LVDT 駆動回路の概略図を図 6.6 に示す。信号発生器より発生させた変調信号はバッファを通して emittor coil に送られ変調磁場を発生させる。今回の試験では変調信号として 10 kHz のサイン波を用いた。誘導起電力により receiver coil に発生した信号が位相ソフト回路を通した変調信号により復調され、ローパスフィルターを通って低周波成分のみが取り出される。今回使用した駆動回路は advanced Virgo 用に NIKHEF で開発されたもので、詳細は [?] に記載されている。

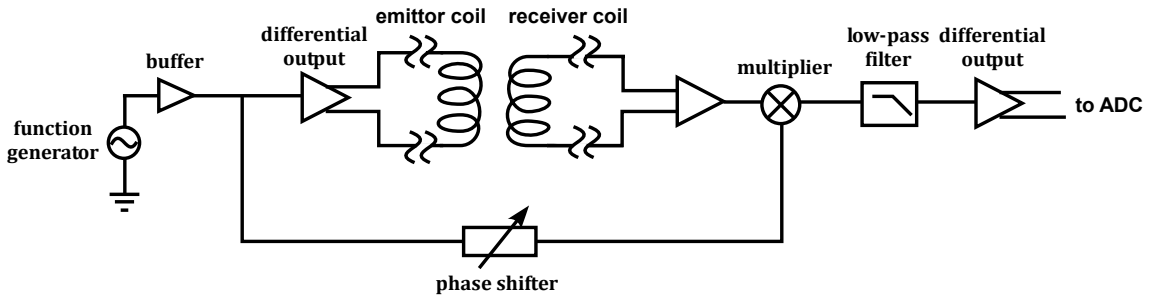

Figure 6.6: LVDT 駆動回路の概略図

1 台の LVDT に関するキャリブレーション結果を図 6.7 に示す。LVDT の出力が 0 となる点より ±5 mm の範囲内で LVDT は線形な応答を示しており、およそ 2 V/mm の感度が得られている。

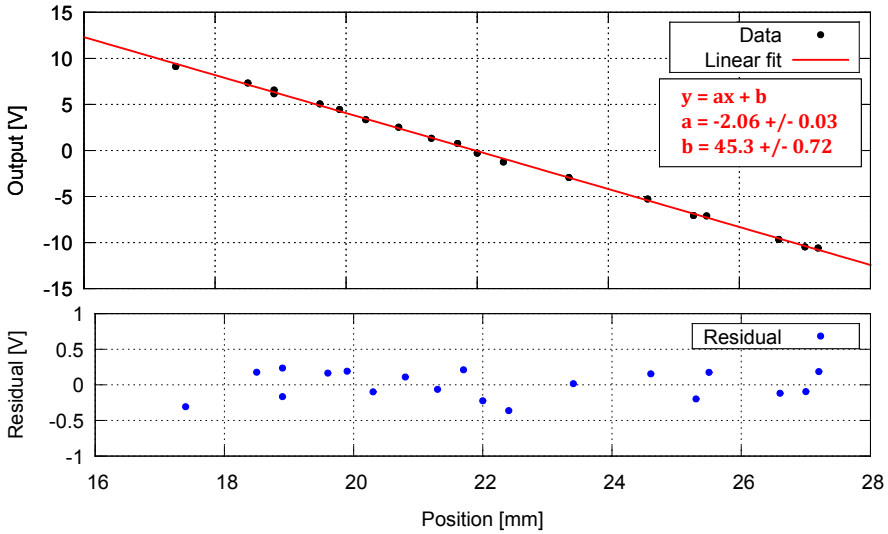

Figure 6.7: LVDT のキャリブレーション結果

ステージを固定した状態での LVDT の雑音スペクトルを測定結果を図 6.8 に示す。LVDT の雑音はデジタルシステムのデータ取得系の雑音 (ADC の量子化雑音) により制限されており、測定された雑音のスペクトル密度は 10 Hz において 4 μV/$\sqrt{\text{Hz}}$、変位換算で 2 nm/$\sqrt{\text{Hz}}$ であった。

Geophone

高周波においてトップステージの振動を制御する際、地面振動雑音の再導入による防振比悪化を防ぐため制御には地面振動を参照しない慣性系に対するセンサーが用いられる。今回の制御試験では Mark Product 社の geophone L-4C を使用した。Geophone は電磁誘導を利用して振動子の振動を読み出す型の地震計で、外部からの制御を必要としない受動的なセンサーである。振動子の共振周波数よりも高い周波数において出力電圧は地面振動の速度に比例する。Geophone の地面振動速度に対する周波数応答は以下の式で表される。

$$H_{\text{geo}}(\omega) = \frac{G\omega^2}{\omega_0^2 + 2ib\omega_0\omega - \omega^2} \tag{6.1}$$

G は速度に対する感度を表し generator constant とも呼ばれる。ω_0 は内部に含まれる振動子の共振周波数、b はその減衰比を表す。典型的な L-4C のパラメータと地面振動の速度に対する周波数応答を表 6.1 および図 6.9 に示す。

Geophone の感度は信号を増幅するためのプリアンプの雑音により主に制限される。今回の試験では advanced Virgo 用に NIKHEF にてデザインされたプリアンプを使用した [?]。図 6.10 にプリアンプの写真および初段の増幅回路を示す。Geophone の信号は初段の増幅回路で約 380 倍に増幅された後、5 倍のゲインでシングルエンドから差動出力に変換され信号取得系に送られる。

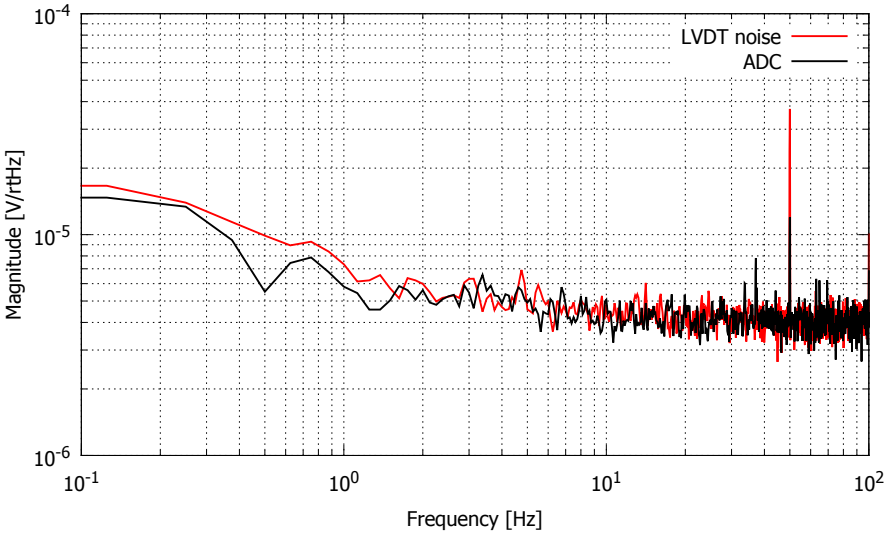

Figure 6.8: LVDT の雑音スペクトルと ADC の雑音の比較

Generator constant (sensitivity)	276 V/(m/sec)
Mass of the oscillator	0.970 kg
Resonant frequency of the oscillator	1.0 Hz
Intrinsic damping ratio	0.28
Coil resistance	5500 Ω

Table 6.1: L-4C の典型的なパラメータ

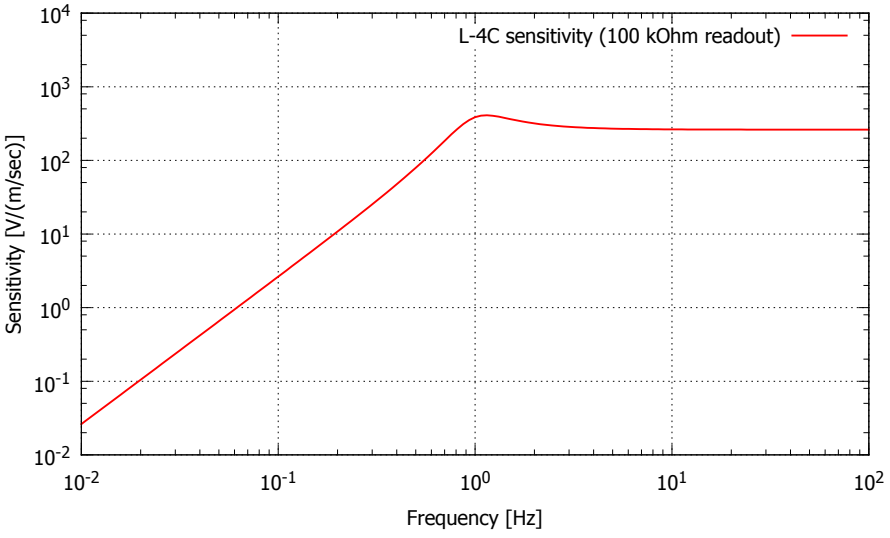

Figure 6.9: L-4C の地面振動に対する周波数応答

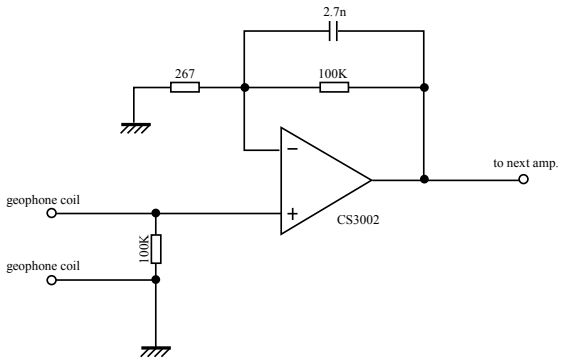

Figure 6.10: Geophone 用プリアンプの写真 (左) および初段の増幅回路の配線図 (右)

プリアンプの雑音は初段の増幅回路のオペアンプ (CS3002) の電圧性雑音および電流性雑音、入力抵抗の熱雑音により決定される。プリアンプの雑音のパワースペクトル $P_{nn}(f)$ は以下の式で計算される。

$$P_{nn}(f) = V_{nn}\left(1 + \frac{f_{cv}}{f}\right) + I_{nn}\left(1 + \frac{f_{cc}}{f}\right)R^2 + 4\pi k_B RT. \tag{6.2}$$

第 1 項がオペアンプの電圧性雑音、第 2 項がオペアンプの電流性雑音、第 3 項が抵抗の熱雑音を表す。ここで R は回路の入力抵抗、k_B はボルツマン定数、T は温度である。オペアンプの電圧性および電流性雑音は低周波で $1/f$ に比例して上昇し、f_{cv} および f_{cc} はその立ち上がり周波数を表す。

図 6.11 にプリアンプ回路の入力換算雑音の見積もりと実測データ（出力電圧のスペクトルを回路のゲインで割ったもの）との比較を示す。雑音測定はプリアンプの入力に L-4C のコイルと同じ抵抗値 (5500 Ω) を持つ抵抗器をつなげた状態で行った。グラフの measurement(1) はプリアンプを大気に露出した状態で測定したもので、measurenet(2) はプリアンプを断熱材で囲まれた箱に入れた状態で測定したものである。Measurement(2) の測定結果は計算結果と良く一致しているが、プリアンプを大気に晒した measurement(1) の測定結果では 1 Hz 以下の低周波でプリアンプ雑音が増大している。原因としては、プリアンプ自身が発生する熱により温度揺らぎが生じ増幅回路内の抵抗値が変動したり熱起電力が生じたりといったことが考えられる。

プリアンプの雑音の測定結果 (measurement(2)) と周波数応答 (図 6.9) から計算される geophone の変位換算雑音と LVDT の変位雑音の比較を図 6.12 に示す。Geophone の雑音は 0.1 Hz 以上で LVDT の雑音レベルを下回るが、振動子の共振周波数以下では急激に雑音レベルが上昇する。

6.2.4 倒立振り子の共振周波数の調整

地面振動の 200 mHz 付近の micro-seismic peak の影響を低減するため、倒立振り子の共振周波数は 100 mHz 以下に下げることが求められる。トップステージに荷重を加えてい

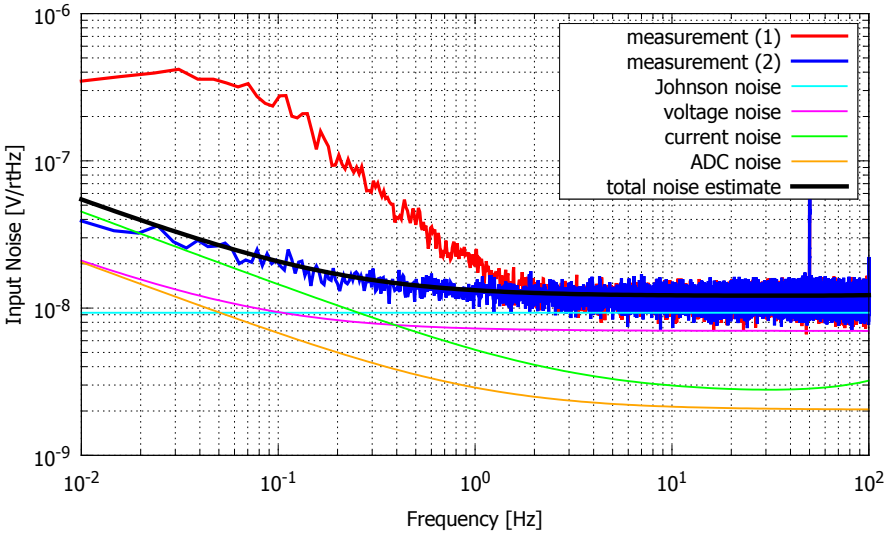

Figure 6.11: プリアンプの入力換算雑音。赤線と青線が実測データ、その他の細線が推定される雑音源のスペクトルを表し、黒い太線がその総和を表す。

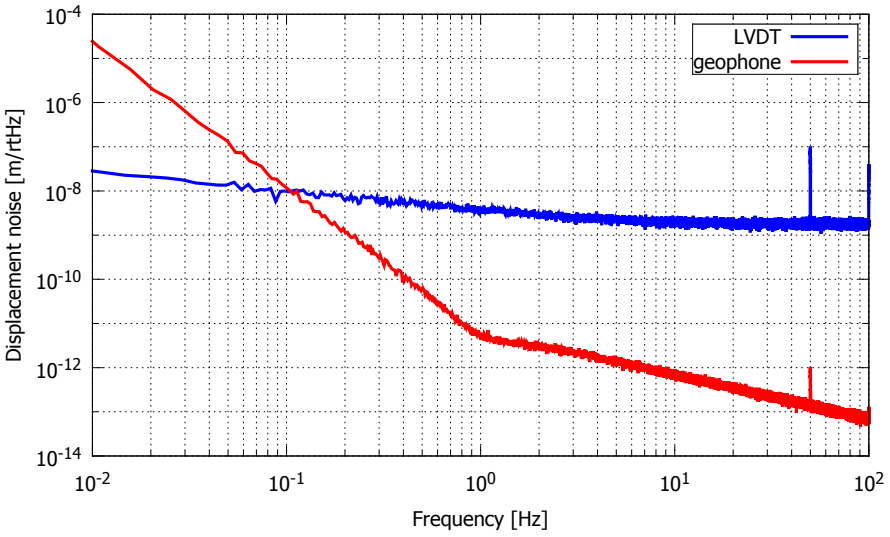

Figure 6.12: Geophone と LVDT の変位雑音レベルの比較

くことで重力による反ばね力が増大し倒立振り子の共振周波数は下がっていく。倒立振り子に荷重を加えていった時の並進モードの共振周波数の推移の測定結果を図 6.13 に示す。

Figure 6.13: 倒立振り子の荷重と共振周波数の関係

トップステージに質量 x のおもりを追加したときの倒立振り子の共振周波数 f_{IP} は以下の式で表される。

$$f_{\mathrm{IP}} = f_0\sqrt{\frac{M_c}{x+M_0}-1} \quad \left(f_0 = \frac{1}{2\pi}\sqrt{\frac{g}{L}}\right). \tag{6.3}$$

ここで L は倒立振り子の脚の長さ、M_0 はおもりを除いたトップステージの質量を表し、今回のセットアップでは $L = 0.48$ m, $M_0 = 310$ kg となっている。この式より共振周波数を 0 Hz とするのに必要な倒立振り子の荷重 M_c をフィッティングにより求めると $M_c = 1108 \pm 4$ kg となる。

6.2.5 座標変換とステージの変位スペクトル

倒立振り子の並進モードの共振周波数を 0.12 Hz に調整した時の、定常状態における各 LVDT の出力のスペクトルと、それを行列 S で変換したステージの座標系における変位スペクトル密度を図 6.14 に示す。各センサーの変位出力 (S_1, S_2, S_3) をトップステージの座標系 (x,y,θ) に変換する変換行列 (S) は以下の式で表される。

$$\begin{pmatrix} x \\ y \\ r\theta \end{pmatrix} = \underbrace{\begin{pmatrix} 1/3 & 1/3 & -2/3 \\ 1/\sqrt{3} & -1/\sqrt{3} & 0 \\ 1/3 & 1/3 & 1/3 \end{pmatrix}}_{\boldsymbol{S}} \begin{pmatrix} S_1 \\ S_2 \\ S_3 \end{pmatrix}. \tag{6.4}$$

ここで r はトップステージの中心からセンサーの位置までの距離を表し、LVDT に対しては $r = 0.7$ m，geophone に対しては $r = 0.5$ m となる。

ステージの座標系に変換することにより共振ピークが分離し、各ピークに対応する共振モードを推定することができる。図 6.14 右下に、この系の剛体モデルから予想される各共振ピークのモードを示す。最も低い周波数の共振は懸架されたダミーマスの鉛直軸周りの回転モードにより生じ、1 本吊りの懸架ワイヤーが捩れる動作に対応する。倒立振り子の動作に対応するのは 0.12 Hz の並進モードと 0.20 Hz の回転モードのピークで、どちらも機械的 Q 値は 10 程度である。0.37 Hz 付近の鋭いピークは懸架されるダミーマスの振り子の共振に対応する。振り子の共振は Q 値が非常に高く、ステージの変位の RMS 振幅に大きく寄与する。

Figure 6.14: LVDT により測定されたステージの変位スペクトルと共振モードの同定

6.2.6 アクチュエータの対角化と伝達関数

倒立振り子をトップステージの座標系 (x, y, θ) について制御するためには、それぞれの向きにステージを駆動するためのアクチュエータへの入力信号の配分を知る必要がある。

すなわちステージの各座標に対応する仮想的なアクチュエータの信号を、実際に設置されている 3 台のアクチュエータの入力信号に変換する行列を決定する必要がある。この行列の決定をアクチュエータの対角化と呼ぶ。アクチュエータによって得たいステージの変位を (u_x, u_y, u_θ)、3 台のアクチュエータへの入力信号を (A_1, A_2, A_3) としてアクチュエータの対角化行列 D は以下の式で表される。

$$\begin{pmatrix} A_1 \\ A_2 \\ A_3 \end{pmatrix} = \underbrace{\begin{pmatrix} D_{1,x} & D_{1,y} & D_{1,\theta} \\ D_{2,x} & D_{2,y} & D_{2,\theta} \\ D_{3,x} & D_{3,y} & D_{3,\theta} \end{pmatrix}}_{\boldsymbol{D}} \begin{pmatrix} u_x \\ u_y \\ u_\theta \end{pmatrix}. \tag{6.5}$$

アクチュエータの対角化の手順は以下の通りである。最初に対角化行列 $\boldsymbol{D}$ に適当な成分を与える ($\boldsymbol{D} = \boldsymbol{D}_{\mathrm{init}}$)。このようにして仮に設定された仮想アクチュエータを用いてステージの振動を励起し、ステージの各座標に対する仮想センサーの出力 (x, y, θ) を読み取る。励起には系の持つ共振周波数よりも十分低い周波数 f_D のサイン波を使用する（本実験では $f_D = 10$ mHz を使用)。これにより各座標に対応する仮想アクチュエータから仮想センサーへの周波数 f_D における伝達係数行列 $\boldsymbol{E}$ が求まる。

$$\boldsymbol{E} = \begin{pmatrix} \tilde{x}/\tilde{u}_x & \tilde{x}/\tilde{u}_y & \tilde{x}/\tilde{u}_\theta \\ \tilde{y}/\tilde{u}_x & \tilde{x}/\tilde{u}_y & \tilde{x}/\tilde{u}_\theta \\ \tilde{\theta}/\tilde{u}_x & \tilde{\theta}/\tilde{F}_y & \tilde{\theta}/\tilde{u}_\theta \end{pmatrix}_{f=f_D}. \tag{6.6}$$

得られた行列 $\boldsymbol{E}$ の逆行列を $\boldsymbol{D}$ に掛けることで新たな対角化行列 $\boldsymbol{D}_{\mathrm{new}} = \boldsymbol{E}^{-1}\boldsymbol{D}_{\mathrm{init}}$ を得る。ここで得られた対角化行列により設定された仮想アクチュエータを用いて再び伝達係数を測定し、行列 $\boldsymbol{D}$ をアップデートする。伝達係数行列 $\boldsymbol{E}$ が単位行列に近付くまでこの作業を繰り返す。今回の測定では行列 $\boldsymbol{E}$ の非対角項が 0.01 以下 (自由度間のカップリングが 1%以下) になるまで対角化作業を繰り返した。

こうして設定された仮想アクチュエータから LVDT で測定されたステージの各自由度の変位への伝達関数を図 6.15 に示す。対角化により 10 mHz 付近で自由度間のカップリングが 1%程度に低減されていることがわかる。一方で共振周波数近傍とそれよりも高い周波数ではカップリングは 1%よりも大きくなっている。これは 3 本の倒立振り子の脚が持つ実効的なばね定数に非対称性があり、低周波において対角化されたアクチュエータは純粋な x 軸や y 軸方向の力、z 軸周りの回転トルクを与えるものではないためであると考えられる。

6.2.7 制御フィルター

ステージの変位の RMS 振幅に大きく貢献する振り子の共振を減衰するためのダンピング制御を実施した。使用したサーボフィルターは

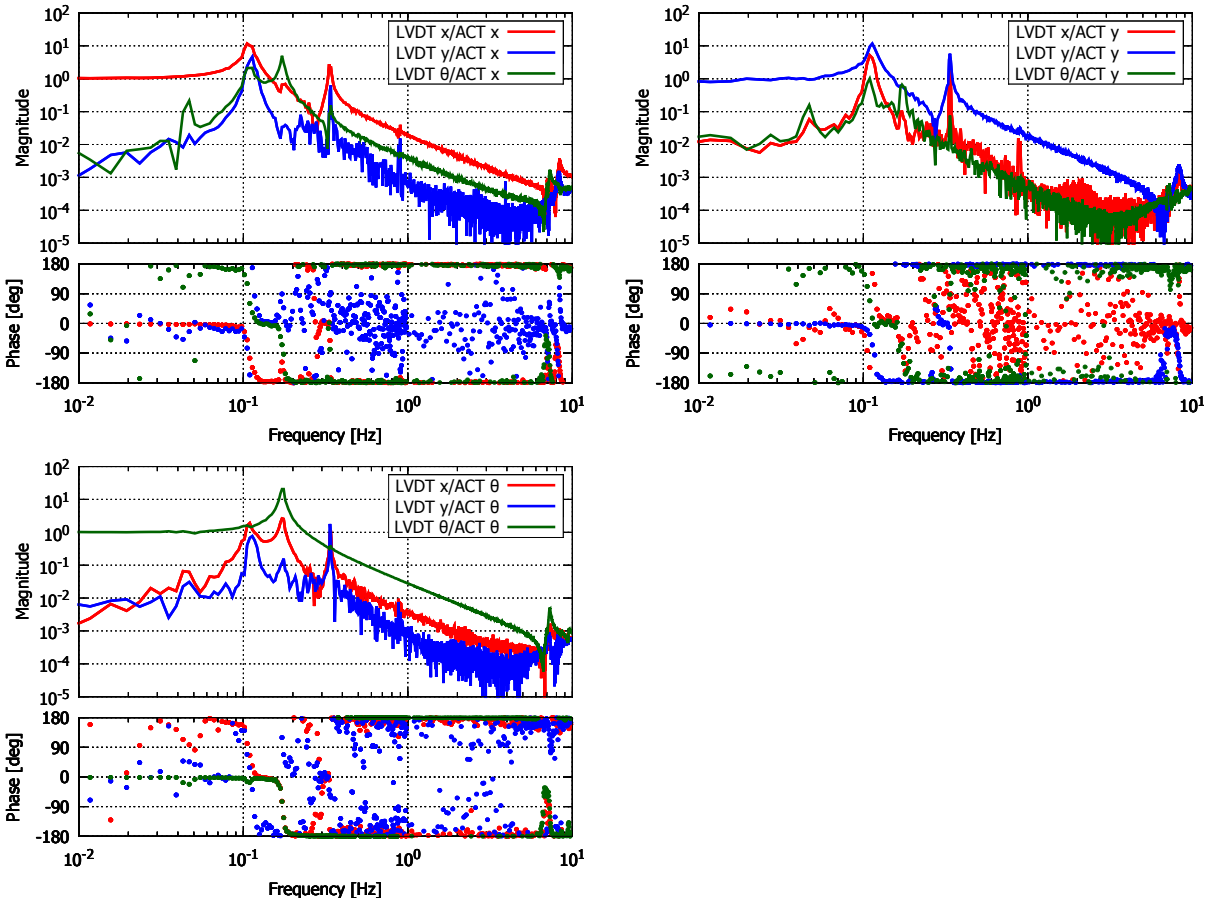

Figure 6.15: 対角化されたアクチュエータから LVDT で測定されたステージ変位への伝達関数

6.3 防振性能の評価

6.3.1 Multi-SAS 用倒立振り子

倒立振り子の防振性能を測るため、地面振動から倒立振り子で支持されたステージの振動への伝達関数の測定を行った。測定に使用した倒立振り子は、ヨーロッパの第 2 世代干渉計型重力波検出器 Advanced Virgo において Multi-SAS と呼ばれる防振系で用いられるものである。Multi-SAS は干渉計のアラインメントを測定するための光学系が搭載される光学ベンチを防振するシステムであり、その基本構造は KAGRA-SAS と良く似ている（図 6.16）。Multi-SAS で用いられる倒立振り子は KAGRA-SAS で用いられるものと同様のデザインであり、今回の測定結果は KAGRA-SAS における倒立振り子の防振特性も示唆する。本実験は Advanced Virgo のための機器開発が行われている研究機関の一つである NIKHEF（オランダ）にて、2013 年 1-3 月の同機関滞在中に行ったものである。

Figure 6.16: multi-SAS の概観

6.3.2 実験セットアップ

図 6.17 に Multi-SAS 用倒立振り子の伝達関数測定のセットアップの写真と概略図を示す。測定の対象となる系は倒立振り子によって支えられるトップステージとそこからワイヤーを通じて懸架されるダミーマスの 2 段振り子構成となっている。測定時、倒立振り子の並進モードの共振周波数は 250 mHz に調整されていた。倒立振り子を支えるベースは金属板ばねにより懸架され、ピエゾアクチュエータを用いて水平方向に加振される。振動を測定するため Wilcoxon 社のピエゾ型加速度計 Model 731-20 をベースおよびトップステージに配置した。加速度計の感度は 10 V/g (2.5 Hz − 2.5 kHz) で雑音レベルはおよそ 0.1 $\mu g/\sqrt{\mathrm{Hz}}$ である。加振と平行な方向の振動を測定するため水平加速度計がトップステージとベースにそれぞれ 1 個ずつ配置し、ベースの傾きを測定するため鉛直加速度計をベースに 2 個配置した。

伝達関数の測定には swept-sine 法を使いた。LabView のプログラムを利用し、励起するベースの振動の周波数を少しずつ変えながら各加速度計の出力電圧の振幅および位相を

比較した。今回測定を行った周波数の帯域は $2-80$ Hz である。測定に使用した加速度計はあらかじめ同じステージ上で加振して出力電圧の差を測定し、測定された出力電圧に係数を掛けることで加速度計ごとの感度の違いを補正した。

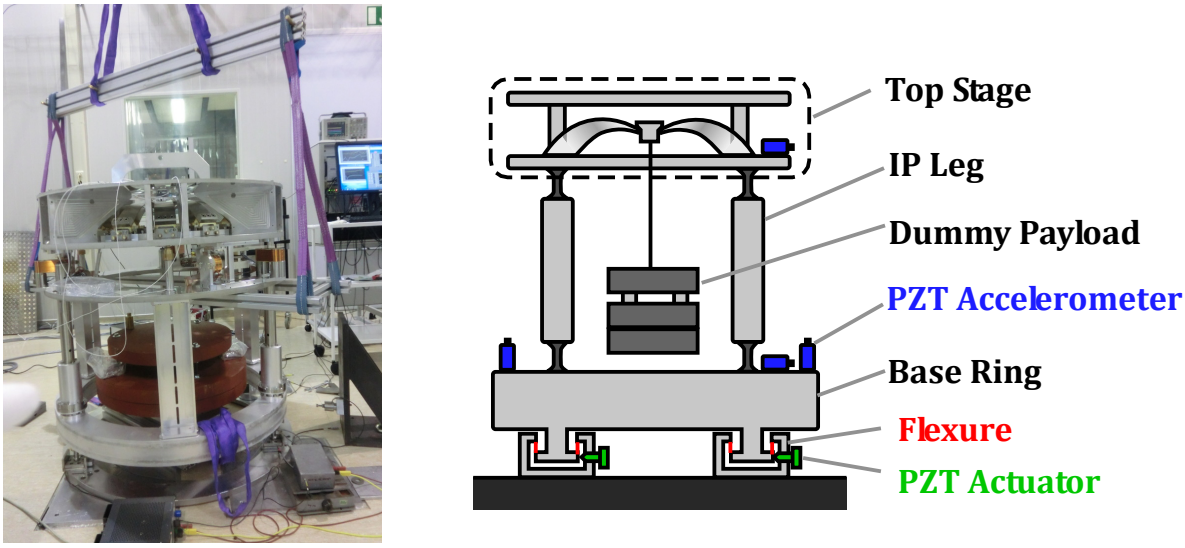

Figure 6.17: multi-SAS 用倒立振り子の伝達関数測定のセットアップ

6.3.3 測定結果

図 6.18 に測定された加速度計の周波数ごとの出力電圧振幅を示す。ベースの傾きはベースに設置された鉛直加速度計の出力の差分を取り計算した。グラフにおいて 68 Hz に現れるピークはベースを支える板ばねの共振によるものである。ピエゾアクチュエータへの入力電圧の振幅は全周波数で一定であり、ベースの変位振幅がほぼ一定であるためベースに設置された水平加速度計の出力電圧の振幅は周波数の二乗に比例している（図 6.18 青線）。トップステージに設置された水平加速度計の出力（図 6.18 赤線）はベースに設置された水平加速度計の出力よりも小さく、倒立振り子による防振効果が確認できる。

ベースの傾きの振幅（図 6.18 緑線）は周波数が上がっていくと急激に上昇し板ばねの共振周波数でピークを迎える。ベースが傾く理由としてはアクチュエータの設置位置とベースの重心位置のズレや、ベースを支持する板バネの非対称性等が考えられる。ベースの傾きは後述するように高周波における倒立振り子の伝達関数測定に影響する。

ベースとトップステージに設置された水平加速度計の出力の比から計算される倒立振り子の振動伝達関数のボーデ線図を図 6.19 に示す。青線は 2 段振り子の質点モデルにより計算される伝達関数の理論曲線で、Center of Percussion 効果による倒立振り子の防振比飽和は -80 dB を仮定している（式**??**における $\beta = -10^{-4}$）。理論曲線に現れる 0.8 Hz のディップと 1.2 Hz のピークはトップステージから懸架される振り子の寄生共振によるものである。

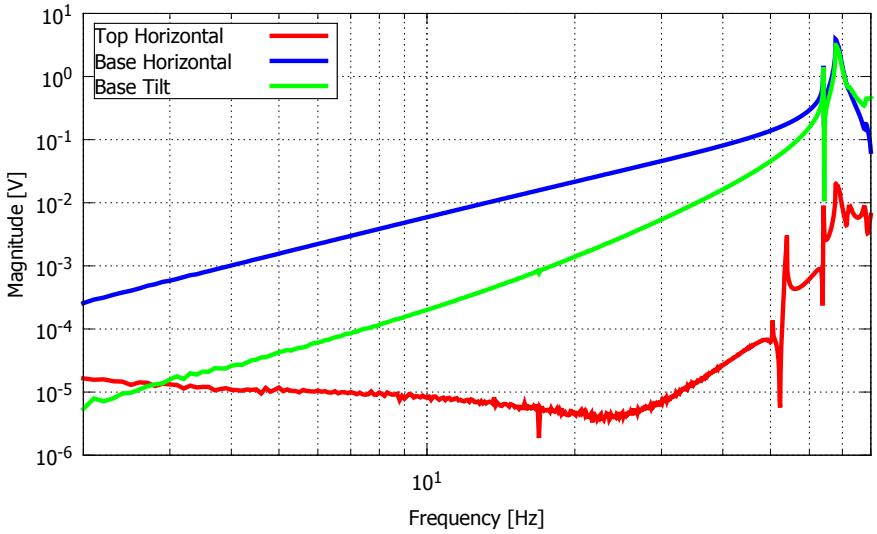

Figure 6.18: 加速度計の周波数ごとの出力電圧振幅

測定された伝達関数は 20 Hz 以下で理論と良く一致しており、最大で −80 dB の防振効果が確認された。一方で高周波では伝達関数の絶対値が上昇していく様子が確認されているが、これは倒立振り子の防振性能が悪化している訳ではなく、後述するベースの傾きからのカップリングによりトップステージに設置した水平加速度計の出力が増大しているためであると考えられる。

6.3.4 傾きによるカップリング

今回の試験では倒立振り子を支持するベースには純粋な水平並進運動だけではなく回転運動（傾き）が生じている。ベースの回転運動がトップステージ上に設置された水平加速度計に与える影響は、1. トップステージの並進運動によるもの と 2. トップステージの回転運動（傾き）によるものの 2 種類に分けられる（図 6.20）。

最初に考えられる影響は、ベースが傾くことで倒立振り子の flex joint の弾性によりトップステージに並進運動が生じ、トップステージに設置された加速度計に出力が生じるものである（図 6.20 左）。ベースの回転角度からステージの変位への伝達関数は図 6.21 の赤線で表される。振り子の共振よりも高い周波数では伝達関数の絶対値は周波数の 2 乗に反比例して落ちていくため、高周波ではこちらの影響は効き難い。

次に考えられる影響は、ベースの傾きによりトップステージが傾くことで加速度計に出力が生じるものである（図 6.20 右）。倒立振り子の脚が軸方向に非常に硬く剛体と見なせる場合、トップステージの回転角はベースの回転角と等しくなる。ステージの回転中心が加速度計と同じ水平面内に無い場合、ステージの回転運動により水平加速度計に出力が生じる。カップリングの大きさはステージの回転中心と加速度計設置位置の高さの差 δh に比例する。倒立振り子の脚を剛体と見なした場合、ベースの傾きから加速度計の位置における水平方向の変位への伝達関数は図 6.21 の青線で示されるように周波数に対してフラットとなり、高周波ではこちらの影響が支配的となる。

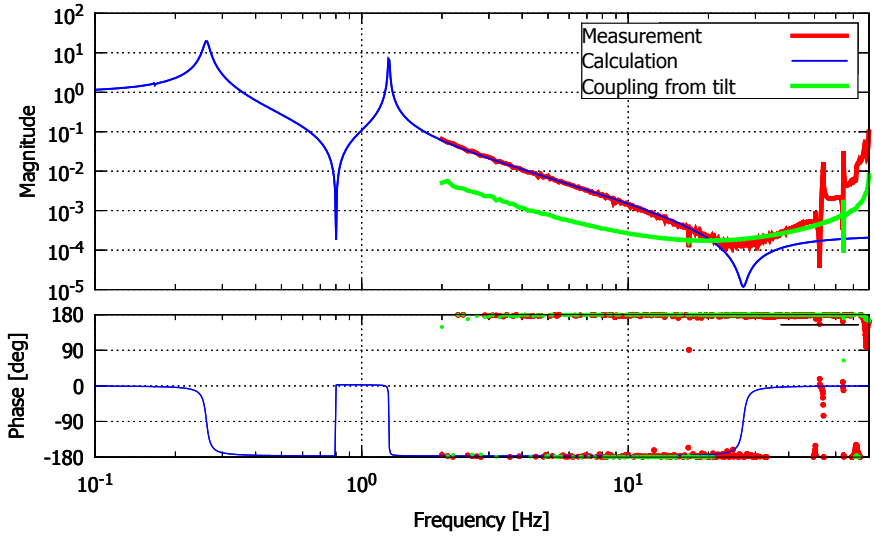

Figure 6.19: Multi-SAS 用倒立振り子の伝達関数

ステージの回転運動からのカップリングは、トップステージに設置された加速度計の位置を調整することにより低減が可能である。図 6.19 で測定された伝達関数は加速度計の高さを最適化した時のものである。図 6.19 の緑線は図 6.21 に示される関数をもとにベースの傾きからのカップリングを計算したものである。ステージの回転中心と加速度計設置位置の高さのずれは $\delta h = 1$ mm としている。計算されたカップリングは 20 Hz 以上の測定結果を良く説明している。

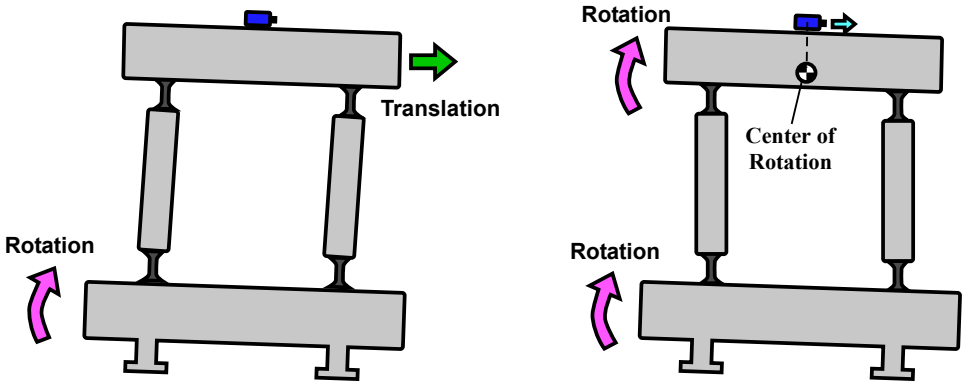

Figure 6.20: ベースの傾きからトップステージ上の水平加速度計へのカップリング

6.3.5 カウンターウエイトの調整

??節で説明した Center of Percussion 効果による防振比飽和を緩和するため、倒立振り子の脚にはカウンターウエイトを取り付けることができるようになっている。カウンター

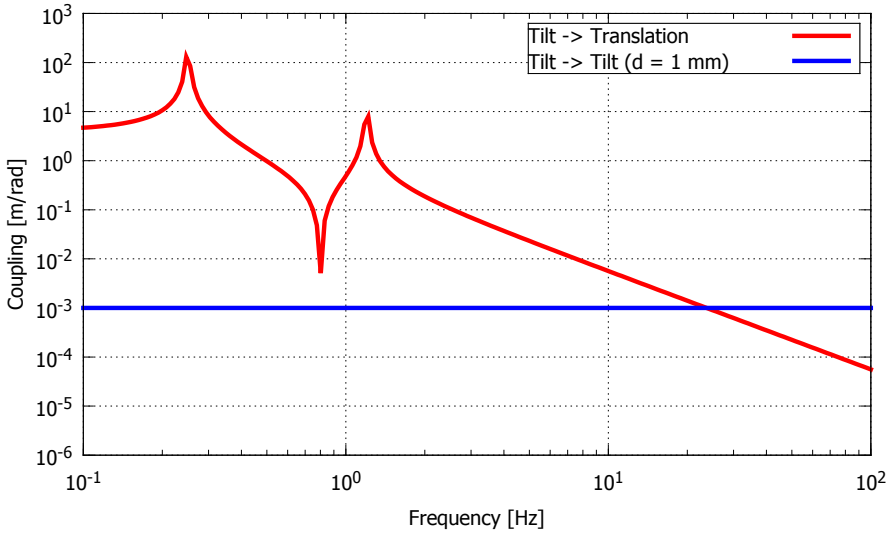

Figure 6.21: ベースの傾き角度からトップステージに設置された水平加速度計の位置における水平変位への伝達関数

ウエイトの重さを変化させた時の 10 – 50 Hz の倒立振り子の防振比の変化を図 6.22 に示す。カウンターウエイトを載せない場合には防振比は-65 dB 程度で飽和するが、カウンターウエイトの重さを調節することで-80 dB 以上の防振比を持たせられることが、この測定結果により示された。

6.4 GAS フィルターの防振性能測定

KAGRA-SAS において鉛直方向防振の要となる GAS フィルターの防振性能を評価するため、加振実験による GAS フィルターの伝達関数測定を実施した。GAS フィルターの防振性能は振動子を構成する板ばねの質量分布のために、倒立振り子の Center of Percussion 効果と同様の効果によって高周波において飽和すると考えられている。この防振比飽和を低減するため、倒立振り子におけるカウンターウエイトと同様の効果を持つ、magic wand と呼ばれる機構が導入される。本試験では伝達関数測定のセットアップを用いて magic wand の調整による防振性能の低減を確認する。

6.4.1 実験セットアップ

GAS フィルターの伝達関数測定のセットアップを図 6.23 に示す。測定を行ったのは KAGRA 用に開発された standard GAS フィルターのプロトタイプである。GAS フィルターのベースをコイルばねを用いて懸架し、電磁アクチュエータにより振動を励起する。GAS フィルターのベースと GAS フィルターより懸架されるダミーマスには鉛直方向に加速度計が取り付けられ、両者の出力の比を取ることにより伝達関数が測定される。使用した加速度計は TEAC 社のピエゾ型加速度計 SA-710 で感度はおよそ 280 $\mathrm{mV/(m/s^2)}$ であ

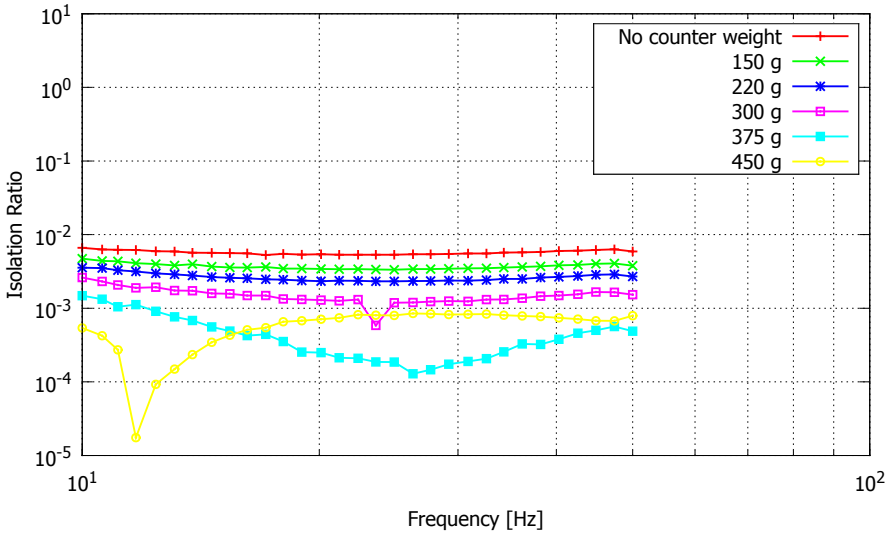

Figure 6.22: カウンターウエイトの重さを変化させた時の倒立振り子の防振比の比較

る。測定には swept-sine 法を用いた。

6.4.2 防振比と magic wand

GAS フィルターの防振性能を向上させるために導入される magic wand の概念を図 6.24 に示す。GAS フィルターに使用される板ばねは質量 m_b および水平軸周りの慣性モーメント I_b を持つものとする。GAS フィルターの中央部に位置する keystone と GAS フィルターのベースを結ぶように質量 m_w，慣性モーメント I_w の剛体棒がヒンジで接続され、magic wand の片端には質量 $M_{\rm cw}$ のカウンターウエイトが固定される。この系における伝達関数は以下の式で表される [?]。

$$H_{\rm GAS}(\omega) = 6\frac{\tilde{z}(\omega)}{\tilde{z}_0(\omega)} = \frac{{\omega_0}^2(1+i\phi)-\beta\omega^2}{{\omega_0}^2(1+i\phi)-\omega^2} \tag{6.7}$$

$$\beta = \frac{1}{M}\left[\frac{m_b l_b(L_b-l_b)}{L_b^2} - \frac{I_b}{L_b^2} + \frac{m_w(L^2-l^2)}{4L^2} - \frac{I_w}{L^2} - M_{\rm cw}\frac{l(L+l)}{L^2}\right] \tag{6.8}$$

ここで M は GAS フィルターが支える質量、$omega_0$ は共振周波数、l_b, L_b, l, L はそれぞれ図 6.24 において定義される長さである。高周波における防振比は $|\beta|$ で飽和する。本試験におけるパラメータを表 6.2 に示す。このパラメータより計算される magic wand が無い場合の防振比の飽和レベルは $\beta \sim 10^{-3}$ である。

6.4.3 測定結果

図 6.26 に GAS フィルターの伝達関数の測定結果を示す。グラフの縦軸は伝達関数の絶対値を表している。Magic wand が無い場合の防振比はおよそ-60 dB で飽和しているが、

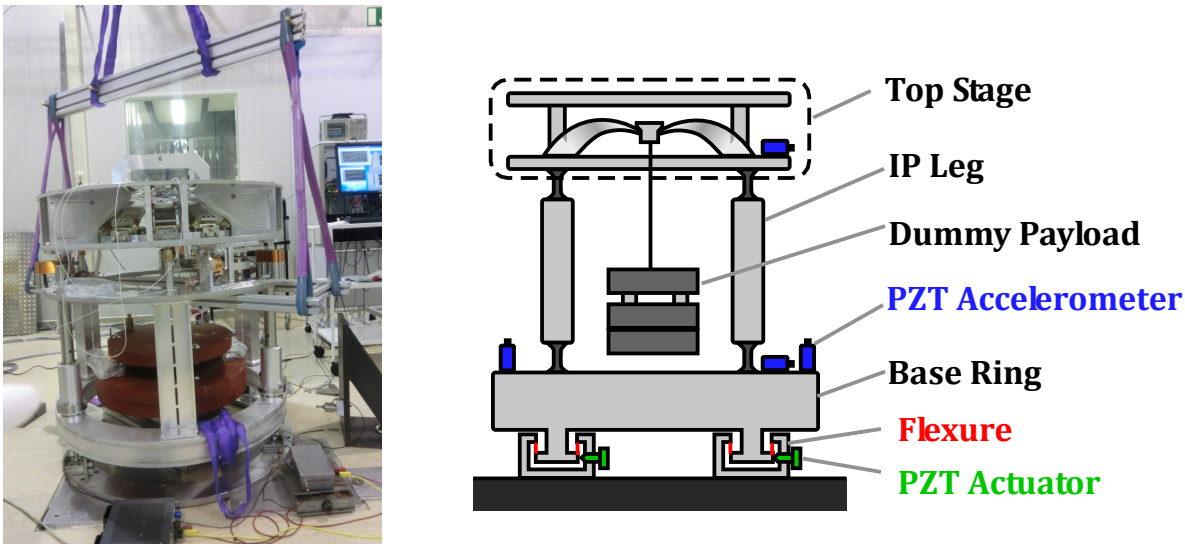

Figure 6.23: GAS フィルターの伝達関数測定のセットアップ

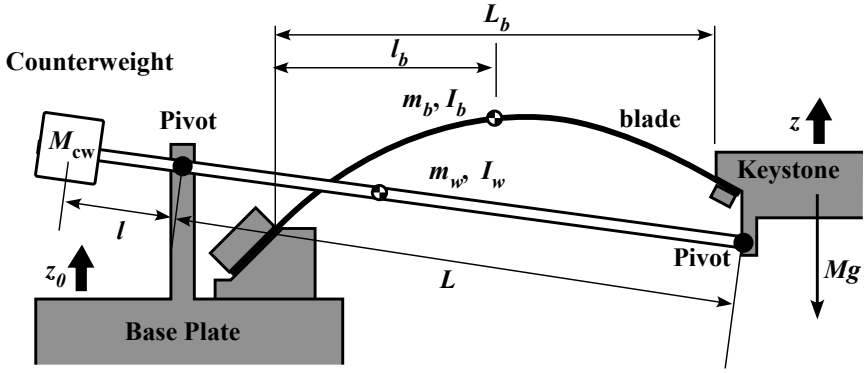

Figure 6.24: Magic wand の概念

M	232 kg
m_b	0.30×6 kg
I_b	0.0065×6 kg m^2
L_b	245 mm
l_b	90 mm
m_w	0.053 kg
I_w	0.0002 kg m^2
L	280 mm
l	50 mm

Table 6.2: Magic wand に関するパラメータ

Figure 6.25: GAS フィルターに配置された magic wand

カウンターウエイトの調整により

Figure 6.26: カウンターウエイト質量と GAS フィルターの防振比の関係

Type-B SAS prototype

Chapter 7

A prototype of the type-B SAS for KAGRA is assembled and tested in the facility of TAMA300, located in Mitaka Campus of National Astronomical Observatory of Japan. The prototype is made for the purpose of checking the assemblability, vibration isolation performance and controllabilty with digital system, and providing feedback on the actual design of vibration isolation systems for KAGRA.

In this chapter, the experimental setups of the type-B SAS prototype are explained in detail. Section 7.1 describes an overview of the experimental setups and associated facilities. Section **??** describes mechanics of the type-B SAS prototype. Section **??** describes sensors and actuators for active controls and some auxiliary sensors as observatories. Section **??** describes digital system and design of control servos.

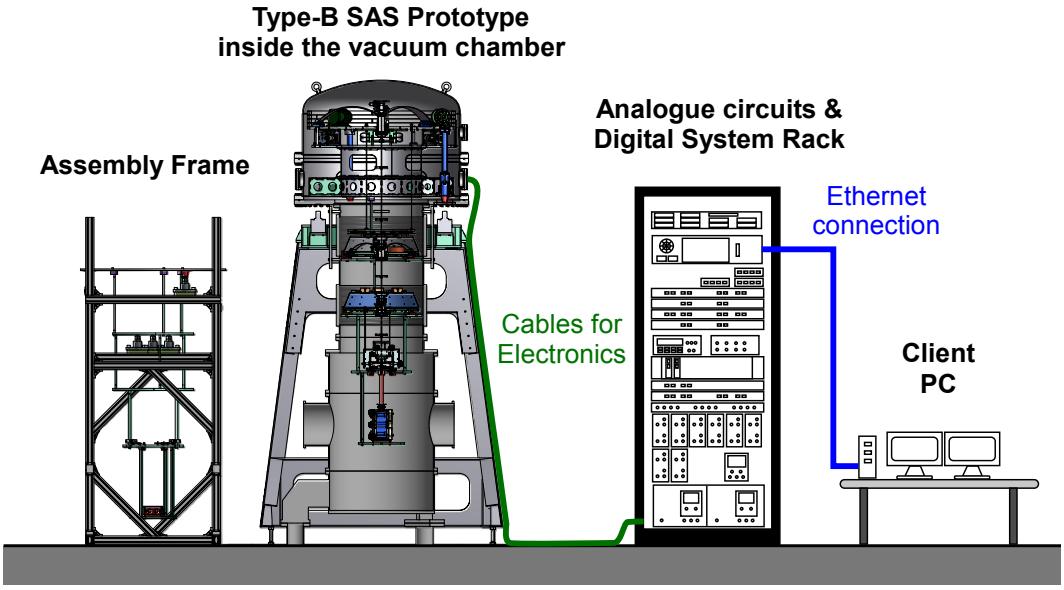

Figure 7.1: A schematic view of the experimental setup for the type-B SAS prototype test.

Figure 7.2: (*Left*) The type-B SAS prototype on an assembly frame waiting for installation into the vacuum chamber seen on the left hand side. (*Right*) A rack containing digital system and analogue circuits for sensors and actuators.

7.1 Overview

A schematic view and pictures of the experimental setup are shown in figures 7.1 and 7.2, respectively. The type-B SAS prototype constructed in TAMA300 is an integrated vibration isolation system with an aluminum dummy mirror suspended instead of an actual silica mirror. The suspension system contains sensors and actuators for active controls, and auxiliary sensors which are implemented only for the performance test. The signals from the sensors and toward the actuators are integrated into digital system placed near the type-B SAS prototype. The digital system applies active controls, actuates the suspension for performance check, and stores data of input/output signals.

The suspension system is assembled on an aluminum assembly frame and then installed into a vacuum chamber next to it. The chamber is evacuated using an oil-free vacuum pump, for reduction of acoustic and air-current noise. Vacuum pressure reaches 4 Pa in 12 hours after pumping starts.

7.2 Mechanical system

An illustration of the type-B SAS prototype and surrounding mechanical components is shown in figure **??**. The main suspension structure locates inside the vacuum chamber and holds a dummy mirror at a height of 1.4 m from the ground. Around the suspension system, there constructed a metal frame which secures the suspension components in case mechanical failue occurs in suspension wires. The base of the suspension system, which locates in the middle of the vacuum envelope, is supported by hydraulic pistons from outside the vacuum chamber. A box containing the hydraulic pistons is supported from the ground by a steel frame surrounding the vacuum chamber.

7.2.1 Suspension system

The type-B SAS prototype consists of five isolation stages and a dummy mirror locates on the bottom of them. The bottom three stages, including the dummy mirror (the test mass; TM), its recoil mass (RM), the intermediate mass (IM), the intermediate recoil mass (IRM) and the bottom filter (BF), are same as the payload prototype described in section **??**. BF is suspended from the standard filter (SF) by a single wire made of maraging steel, and SF is also suspended from the top filter (TF) by a single wire of the same material. For reduction of Q factors about torsion modes of single-wire suspensions, the magnetic damper (MD) is placed above SF to provide damping torque on it. MD is suspended from TF by three wires made of maraging steel. TF is supported from the base structure by three inverted pendulum (IP) legs, whose resonant frequencies are tuned as low as 100 mHz.

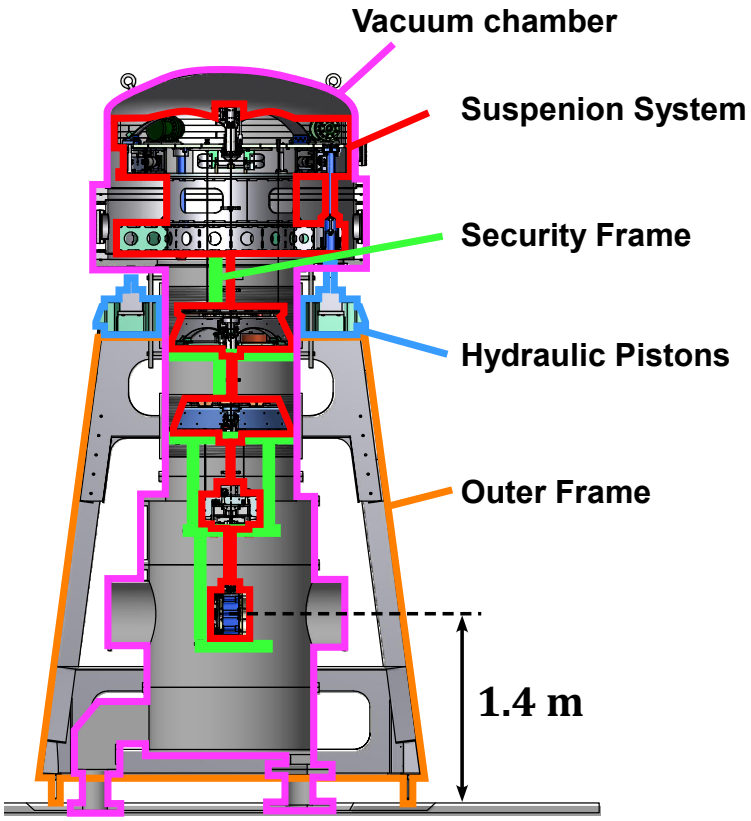

Figure 7.3: A schematic view of the type-B SAS prototype and surrouding mechanical sturctures.

Mass distribution

Table 7.1 shows distribution of mass in the suspension system. As discribed in sections **??** and **??**, performance of GAS filters and inverted pendulums are sensitive to their load, and therefore the mass on each stage must be tuned carefully in about 0.1 kg precision. For the fine tuning of load on GAS filters, small metal discs are placed on top of each stage and the amount of the discs are controlled so that GAS filters are in their nominal working points. Tuning has been conducted from the lower stages since they affect the load on upper stage GAS filters. The discs are also used to balance the tilt of each stage by changing their horizontal positions.

Body	Mass [kg]	GAS/IP	Load [kg]
TM	11.1		
RM	12.5		
IM	26.5	BF	50.1
IRM	8.1		
BF	107.0	SF	165.2
SF	111.0	TF	276.2
MD	17.8		
TF	554	IP	848

Table 7.1: Mass distribution in the type-B SAS prototype.

7.2.2 Support of suspension system

Figure 7.4 shows an extended view around the boundary between the base of the suspension system and a hydraulic piston. The base is supported by cone shape adapters placed just below IP legs, and each adapter sits on a hydraulic piston actuated by oil pump. The adapters are welded to metallic bellows which separates the vacuum part (on the side of the suspension system) and the in-air part (on the side of the pistons).

The bellows also works as mechanical isolators separating the vibration of the suspension system from that of the vacuum chamber. Since the vacuum chamber has huge mass and its support is not robust, vibration of the chamber tends to be enhanced by mechanical resonances at low frequencies (few Hz). This may degradate performance of SAS and thus mechanical isolation between the chamber and the suspension system is mandatory.

The ground vibration is transmitted to the suspension system through the outer frame surrounding the vacuum chamber. The rigidity of the outer frame is essential since its mechanical resonances can enhance the vibration of the IP base and degradate the pefromance of SAS. In addition, flexibility of the outer frame causes back-action in the actuators on the top stage, and thus can cause instability of active controls. It is important to push the resonant frequencies as high as possible, at least higher than the bandwith of the IP

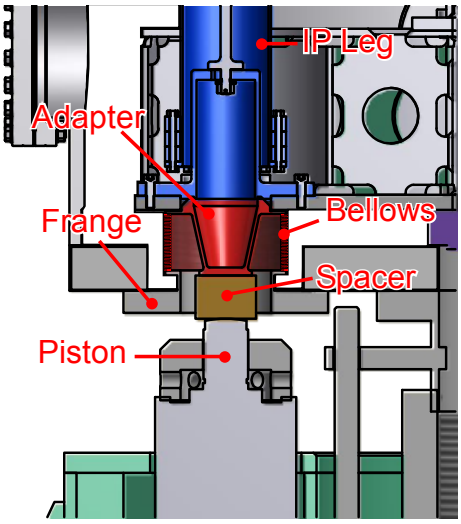

Figure 7.4: A drawing of the boundary between the IP base and a hydraulic piston.

active controls ($\sim$ 1 Hz). According to an FEM simulation on the currently designed outer frame, the resonant frequency of the lowest-order resonant mode (the mode shape is illustrated in figure 7.5) is $\sim$8 Hz, assuming 1400 kg load on top of the frame.

Figure 7.6 shows measured vibration spectrum on top of the outer frame, compared with that on the floor. Amplitude ratio of two spectra is also shown in the lower graph. The measurement shows that, in high frequency region, the amplitude of the outer frame vibration gets 1-2 orders of magnitude larger than that of the ground vibration, probably due to mechanical resonances and pickup of acoustic noise. A large peak at 8.8 Hz would correspond to the lowest-order resonant mode of the outer frame.

7.2.3 Security frame

Figure 7.7 shows an illustration of the security frame designed for the type-B SAS prototype. Below each stage of the suspension chain, there placed a metal disc to secure the suspended masses in case they drop due to mechanical failure in suspension wires. The discs holds range limiter which restricts the displacement of the suspended mass into few millimeters during the operation. They also contain locking mechanism used when the assembled system is transported.

Discs are connected to the IP base by metal pillars with enough thickness so that they can hold the weight of suspension system in case of accidents. Basically the diameters of the pillars are set 25 mm in design, however, in the prototype system, the diameters of the pillars connecting upper two stages are reduced to 15 mm, because of limited space in the vacuum envelope. The resonant frequency of the lowest-order mode is as low as 3 Hz according to an FEM simulation (see figure 7.7). The frequency increases to 7 Hz when the pillars on the two stages are replaced to those in 25 mm diameter. Although the flexibility of the security frame does not affect the vibration isolation performance of SAS

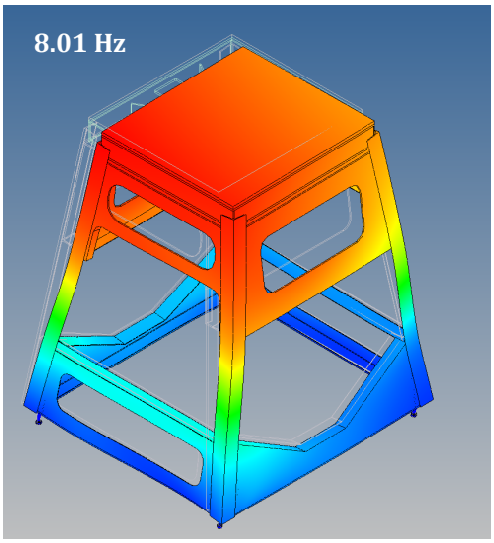

Figure 7.5: An illustration of the lowest-order resonant mode of the outer frame w predicted from an FEM simulation. The simulation assumes $\sim$ 1400 kg load on top of the frame.

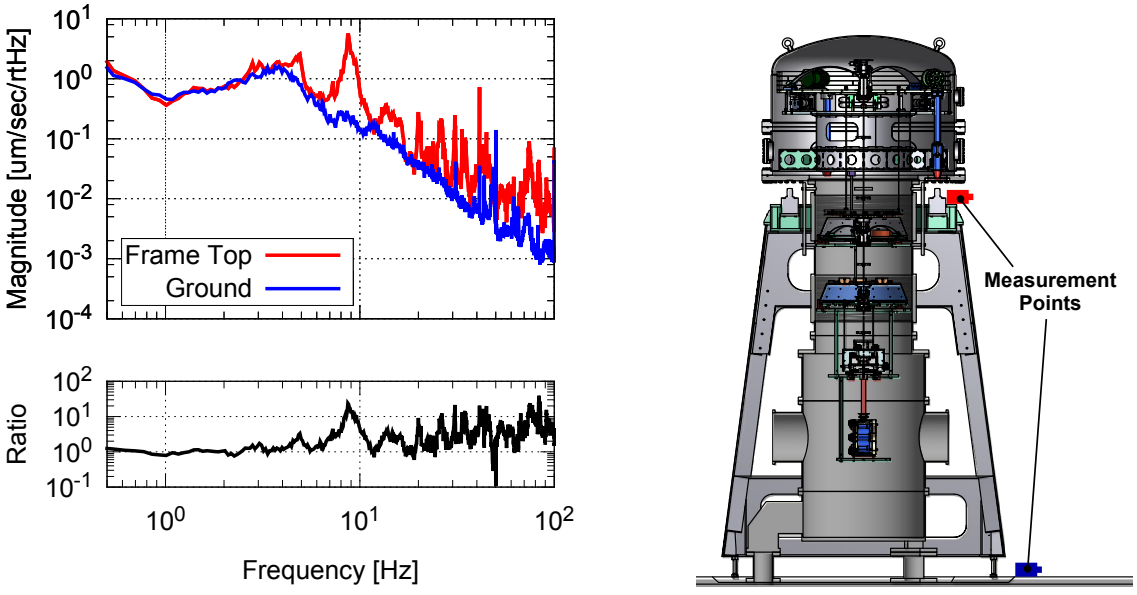

Figure 7.6: Comparison of horizontal vibration spectrua on the floor and on top of the outer frame in velocities, measrured by a geophone L-4C. Amplitude ratio of two spectra ($\tilde{x}_{\rm frame}/\tilde{x}_{\rm floor}$) is shown in the lower graph.

itself, its vibration may introduce scattered light noise in the interferometer and must be treated carefully in the actual system.

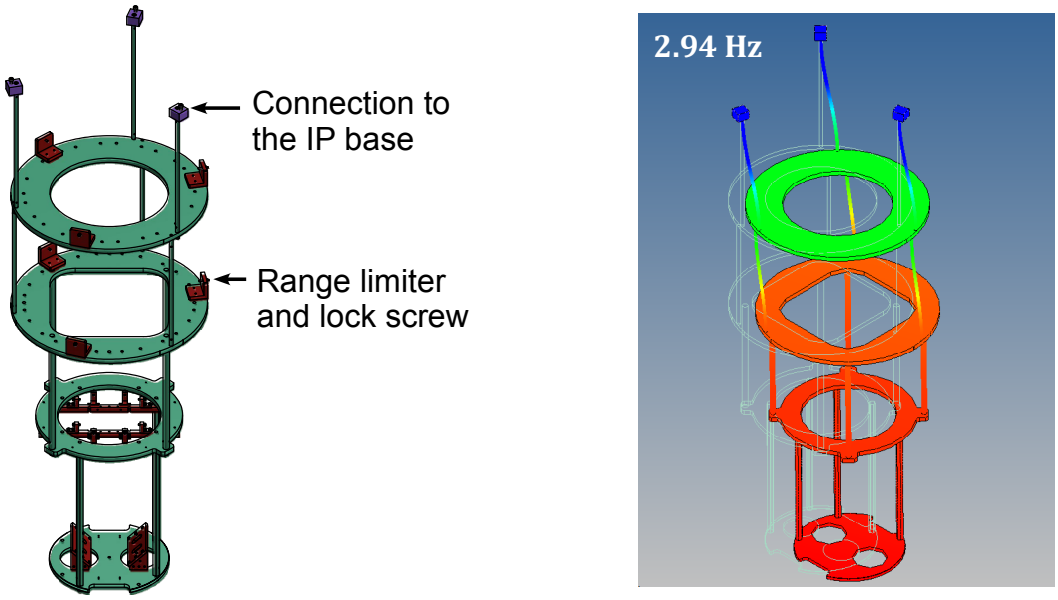

Figure 7.7: An illustration of the security frame for the prototype system (*left*) and its lowest-order resonant mode shape (*right*).

7.3 Sensors and actuators

7.4 Digital control system

7.5 Sensing and control scheme

7.6 Suspension assembly

Performance test of type-B SAS prototype

Chapter 8

8.1 Overview

We conduct performance test of the KAGRA type-B SAS prototype. In sec. 8.2, the mechanical response of the suspension system without active control is checked by using implemented sensors and actuators. We conduct the test to confirm if the suspension system behaves as expected from the simulation. We see the deviation from simulated results and feed it back to the servo design of active control system.

In the sections after sec. 8.3, we conduct tests on the active control system. As discussed in 8.3, the state of the detector is categorized into three phases (the calm-down, lock-acquisition, and observation phases) and we have different control loops in each phase. In sec. 8.3, we forcus on the damping controls in the calm-down phase and check if the suspension system goes back to the operatation status in short time. In sec. 8.4 and **??**, we perform low-RMS controls for the lock-acquisition phase. We describe on the IP controls using blended sensor signals, and angular controls of TM using the optical lever. In sec. **??**, we demonstrate the lock of TM longitudinal displacement using photo-sensors as substitution for a laser interferometer. Several control loops are switched off to reduce the control noise and we investigate the noise coupling from remaining control loops in the observation frequency band ($> 10Hz$).

In sec. **??**, we perform long-term test of active controls to demonstrate the stability of the system. We succeed in keeping the lock of TM displacement for 5 days, except for one lock failure due to an earthquake.

8.2 Frequency response of mechanical system

In this section, mechanical response of the type-B SAS prototype is investigated by using implemented sensors and actuators. We compare the measured frequency response

with simulation results and check if the mechanical system works as is designed.

8.2.1 Measurement setup

The measurement has been done by injecting broadband gaussian noise from actuators in a certain degree of freedom and checking the resulting displacements measured by sensors. The noise injection point and measurement point in the digital system are shown in the block diagram in Fig. 8.1. Transfer functions are calculated as $H(\omega) = \tilde{x}/\tilde{n}$.

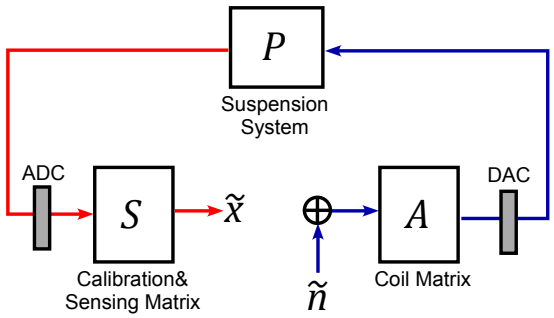

Figure 8.1: Signal flows in the transfer function measurement.

The virtual actuators to which the noise is injected are diagonalized beforehand. The actuator diagonalization about the IM and TM stage is conducted using the method described in section 7.5 with sinusoidal excitation at a frequency well below the resonant frequencies regarding the mass to be actuated. The diagonalization frequencies are set 20 mHz both for the actuators on IM and TM. On the other hand, we do not use the same diagonalization scheme for the actuators on F0. Due to large couplings between different DoFs, the frequency response to the virtual actuators diagonalzed with this scheme gets complicated, and that makes the SISO-type control quite difficult. Thence the coil matrix for the F0 actuators is roughly set from geometry, and then is normalized so that the amplitudes of diaognal transfer functions from the actuators to the sensor signals become 1 in DC.

Amplitude and spectrum of the excitation signal are tuned so that we obtain sufficient S/N in the whole interested frequency band but do not excite the mechanical resonances much, to let the sensors staying in the linear regime. Excitation amplitude is reduced around 1 Hz where many resonant frequencies of the suspension system exist and notch filters are introduced for some specific resonances. The left graph in Fig. 8.2 shows an example of spectra of the excitation in the TM longitudinal direction and displacements measured by OSEMs on TM. A notch filter is introduced to the excitation signal at 0.66 Hz, which is the resonant frequency of the pendulum mode about TM and RM. The right graph shows the coherence between the excitation signal and measured displacement signals. Good coherenence is observed between the excitation signal and longitdinal displacement

in a wide frequency band, while poor coherence is observed around resonant frequencies because of disturbances from seismic vibration.

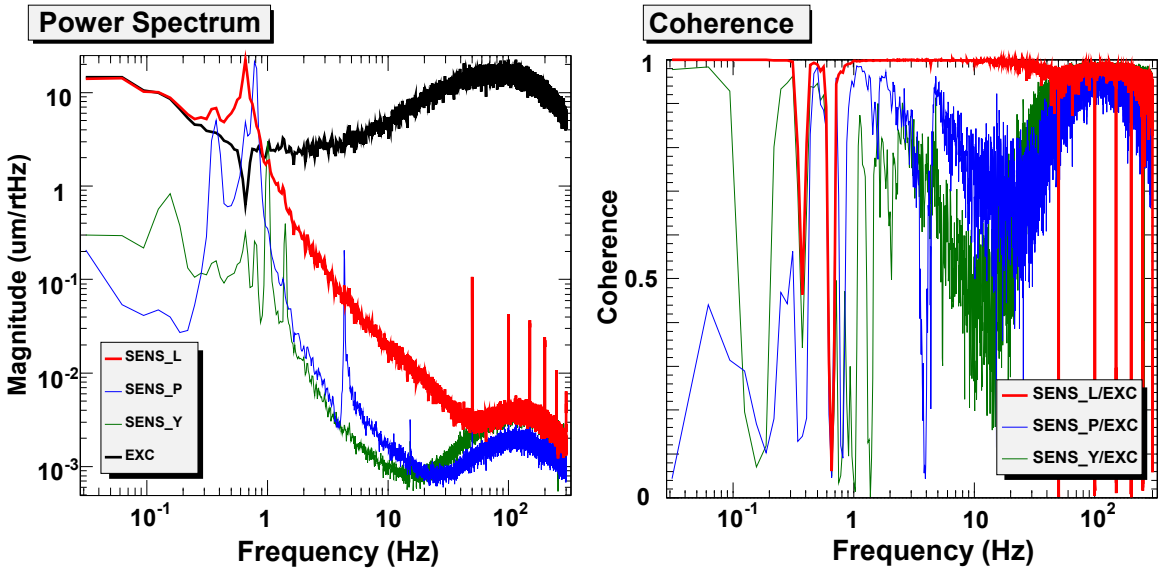

Figure 8.2: (*Left*) Spectra of the excitation signal in the TM longitudinal DoF and measured displacement signals. (*Right*) Coherence between the excitation signal and sensor signals.

8.2.2 Frequency response in TM stage

Mechanical response of the TM and RM suspension is investigated by using 4 OSEMs impltemented on them. The OSEMs excite and measure the reletive displacement or rotation angle between TM and RM in 3 DoFs; longitudinal(L), pitch(P) and yaw(Y). Transfer functions from the actuation about these 3 DoFs to the displacements are shown in Fig. 8.3. Note that only diagonal parts (e.g. from longitudinal excitation to longitudinal displacement) are shown here. The black curve in each graph shows the predictuion from rigid-body model simulation.

Measured transfer functions fit very well with the prediction at low frequencies, while they start to deviate at around 30 Hz. The larger couplings observed in actual system are due to direct electro-magnetic coupling between the actuation signal and sensor signals through cables. The cables going to actuator coils and those coming from sensors form capacitance which transmits high frequency components of excitation signals directly. Though the amplitude of the coupling should be proportional f, it is suppressed by a first-order low-pass filter implemented in the driver circuit with a cut-off frequency at 100 Hz. Thence the amplitudes of the transfer functions show flat frequency response at high frequencies.

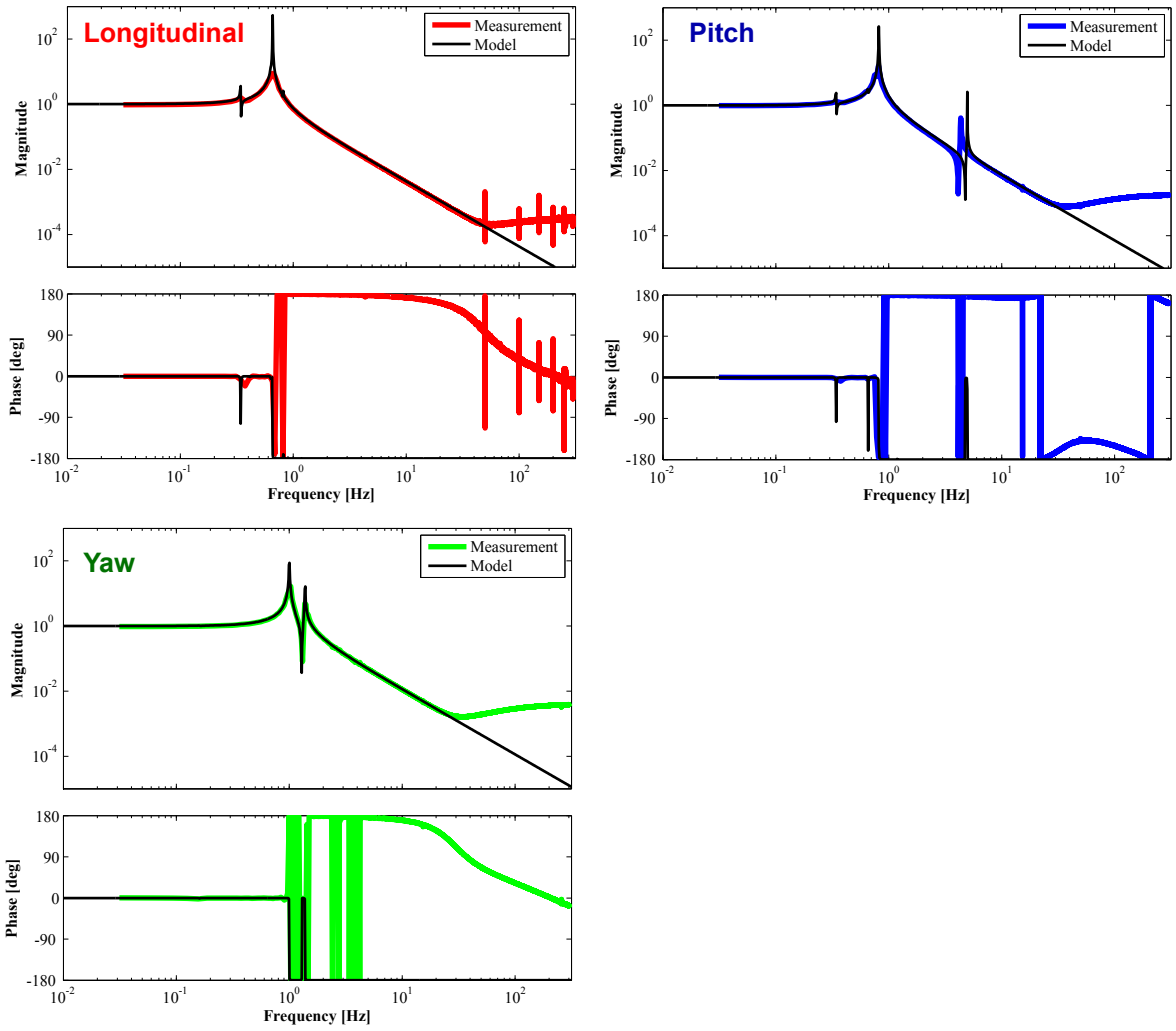

Figure 8.3: Comparison of measured transfer functions about TM and prediction from the rigid-body model simulation.

Another deviation between the meausrement and simulation is the position of the pitch resonant peak at around 5 Hz. The peak corresponds to the resonance about pitch mode of RM. The simulation predicts the resonant frequency at 4.9 Hz while the measured resoanant frequency is 4.3 Hz. A possible reason is that the hanging condition of RM is not good and one of the 4 wires suspending RM is not loaded. The floating wire doesn't contribute to the stiffness in the RM pitch motion and the spring constant is reduced by 25%. Consequently the resonant frequency of pitch mode is reduced by 13%, which is consistent with the observed deviation. This assumption predicts that also the resonant frequencies about the RM vertical and roll modes are reduced, which is actually observed in the frequency response of the IM stage (see the next subsection).

8.2.3 Frequency response in IM stage

Mechanical response in the IM-IRM stage is investigated by using 6 OSEMs implte-mented on them. The OSEMs can excite and sense the rigid-body motions of IM and IRM in 6 DoFs. Measured diagonal transfer functions and the comparison with the prediction are shown in Fig. 8.4.

Frequency responses in the IM stage becomes rather complicated since there exist backaction from the TM and RM suspension. Again measured transfer functions fit well with the prediction while they deviate at high frequencies due to electro-magnetic coupling between the actuators and sensors.

Another outstanding deviation is the existence of resonant peaks which are not predicted from the simulation or have different frequencies from those in the prediction. Resonant peaks found at 45 Hz in vertical, 57 Hz in roll and 4.3 Hz in pitch are related to the boucing mode of suspension wires for RM. As described in previous subsection, measured frequencies of these modes are lower than prediction, probably due to a floating wire. Resonances found around 70-80 Hz in roll and pitch transfer functions are expected to be violin modes of the RM suspension wires.

8.2.4 Frequency response in F0 stage

Mechanical response in the F0 stage is investigated by using 3 LVDTs and 3 geophones implemented on the F0 stage. The signals from LVDTs and geophones are blended at 100 mHz and are then converted to displacement of the top stage in 3 DoFs; longitudinal (L), transversal (T) and yaw (Y). Measured diagonal transfer functions and the comparison with the predictions are shown in Fig. 8.5.

The response about translation modes fits well with the prediction at high frequencies (¿ 0.1 Hz), except for the existence of resonant peaks around 20 Hz. The resonances corresponding to these peaks are not found in the rigid-body model of the suspension system. The peaks could relate with mechanical resonances of the external frame supporting the system, which might be coupled with the sensor signals through the tilt of the suspension base caused by the reaction from the actuators.

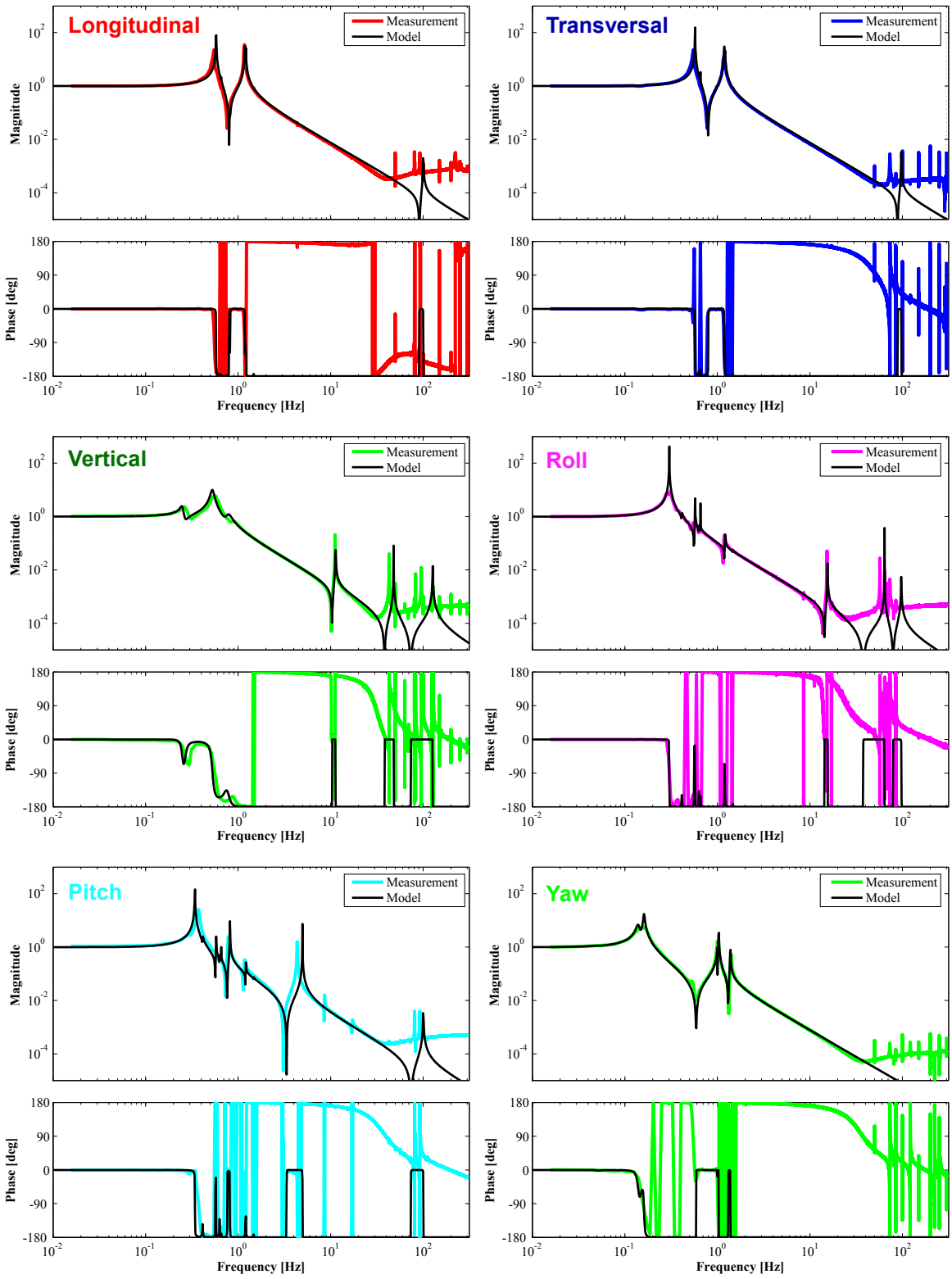

Figure 8.4: Comparison of measured transfer functions about IM and prediction from the rigid-body model simulation.

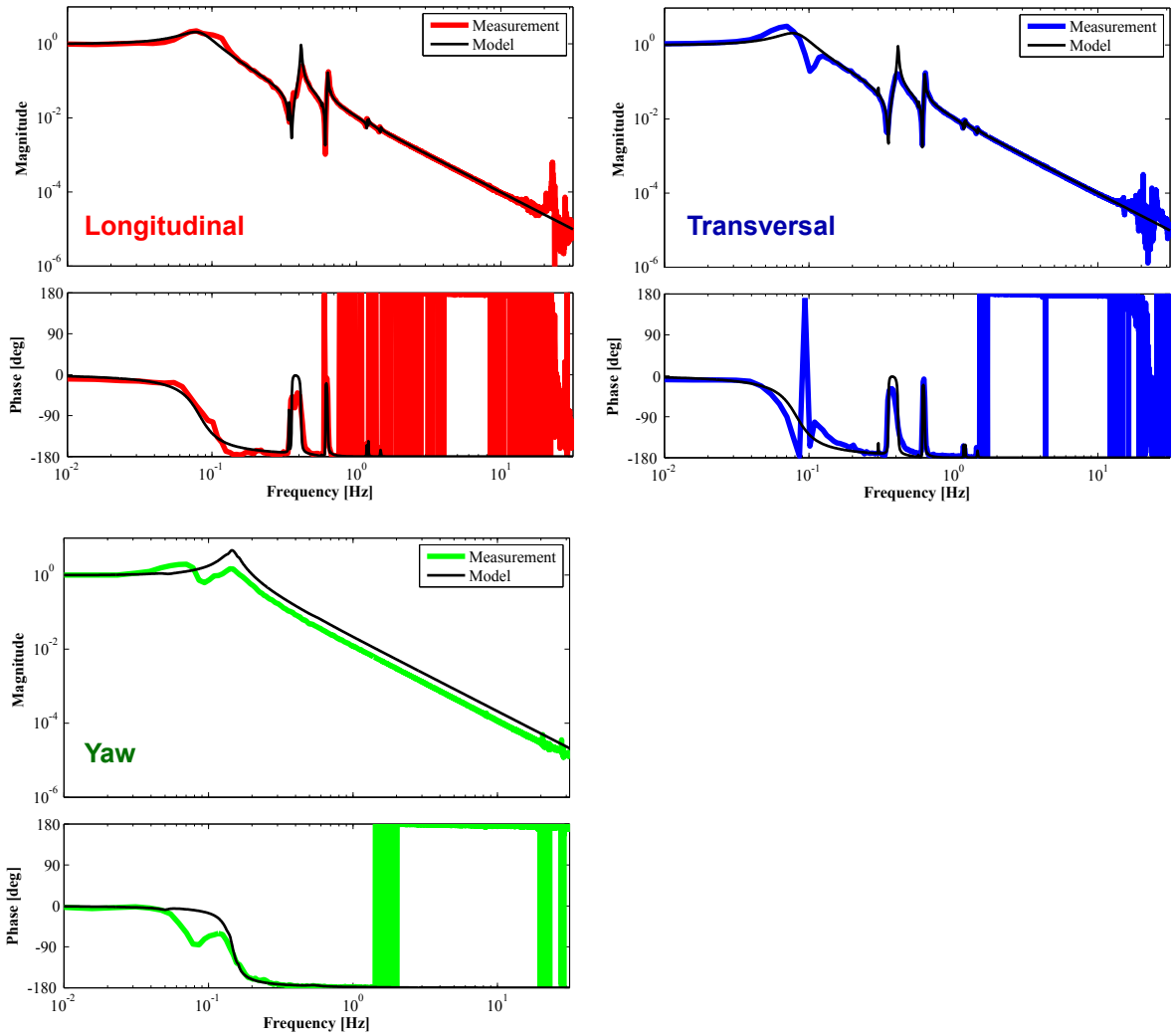

Figure 8.5: Comparison of measured transfer functions about F0 and prediction from simulation. The simulation does not take into account any asymmetry in the IP stiffness.

The frequency responses at low frequencies in transversal and yaw modes deviates largely from those in the simulation. The deviation can be explained by asumming asymmetry in the IP stiffness and large couplings between the transversal and yaw motions. Actually the resonant peak corresponding to the transversal mode of IP is also found in the transfer function in yaw, and vice versa. The simulated frequency response shown in Fig. 8.5 doesn't take into account this asymmetry.

8.2.5 Frequency response of GAS filters

The frequency responses of GAS filters are measured by implemented coil-magnet actuators and LVDTs. Fig. 8.6 shows the measured transfer functions and comparison with the prediction. Respective resonant frequnecies of the GAS filters are measured by fixing other GAS filters mechanically and seeing oscillation signals with impludive excitation. Measured resonant frequencies are 0.33, 0.38 and 0.44 Hz for F0, F1 and F2 respectively. We use these values in the simulation. Measured resonant freuqnecies in the coupled system are higher than the prediction by $\sim$10%. This might be because the measurement is conducted in different working points of GAS filters.

Amplitude of the measured transfer functions raise above few Hz. This is caused by magnetic-field coupling between the coil-magnet actuator and LVDT. The coaxial LVDT coils sense the magnetic field produced by the actuator coil and thence the actuation signal directly transmits to the sensor signal at high frequencies. Although the effect by magnetic field is mitigated by modulation-demodulation scheme in the LVDT signal extraction, still the effect is non-negligible and it produces false signals on LVDTs. Due to this raise of transfer function magnitude, the feedback control using these sensors and actuators cannot be applied with bandwidth higher than 1 Hz, but it does not make any problems in our use.

8.2.6 Couplings with other DoFs

The measurement results described above only show the diagonal transfer functions, looking at the same DoFs as those of the excitation. Here the couplings between other DoFs are discussed.

Fig. 8.7 shows the transfer functions from the actuators about the TM-RM longitudinal mode to the TM-RM motions including other DoFs than longitudinal. Since the actuators are diagonalized at 20 mHz, amplitudes of the off-diagonal transfer functions are much lower than that of the diagonal one (few %) at low frequencies. On the other hand, the transfer functions at the frequencies higher than resonances show larger coupling ($\sim$10% at 10 Hz).

The following tables show magnitude of coupling coefficients (amplitudes of transfer functions) at a low frequency (10 mHz) and a high frequency (10 Hz). The response about IM and TM actuators shows small coupling to other DoFs at the low frequency owing to the actuator diagonalization. In the meanwhile, the response of IM actuators shows

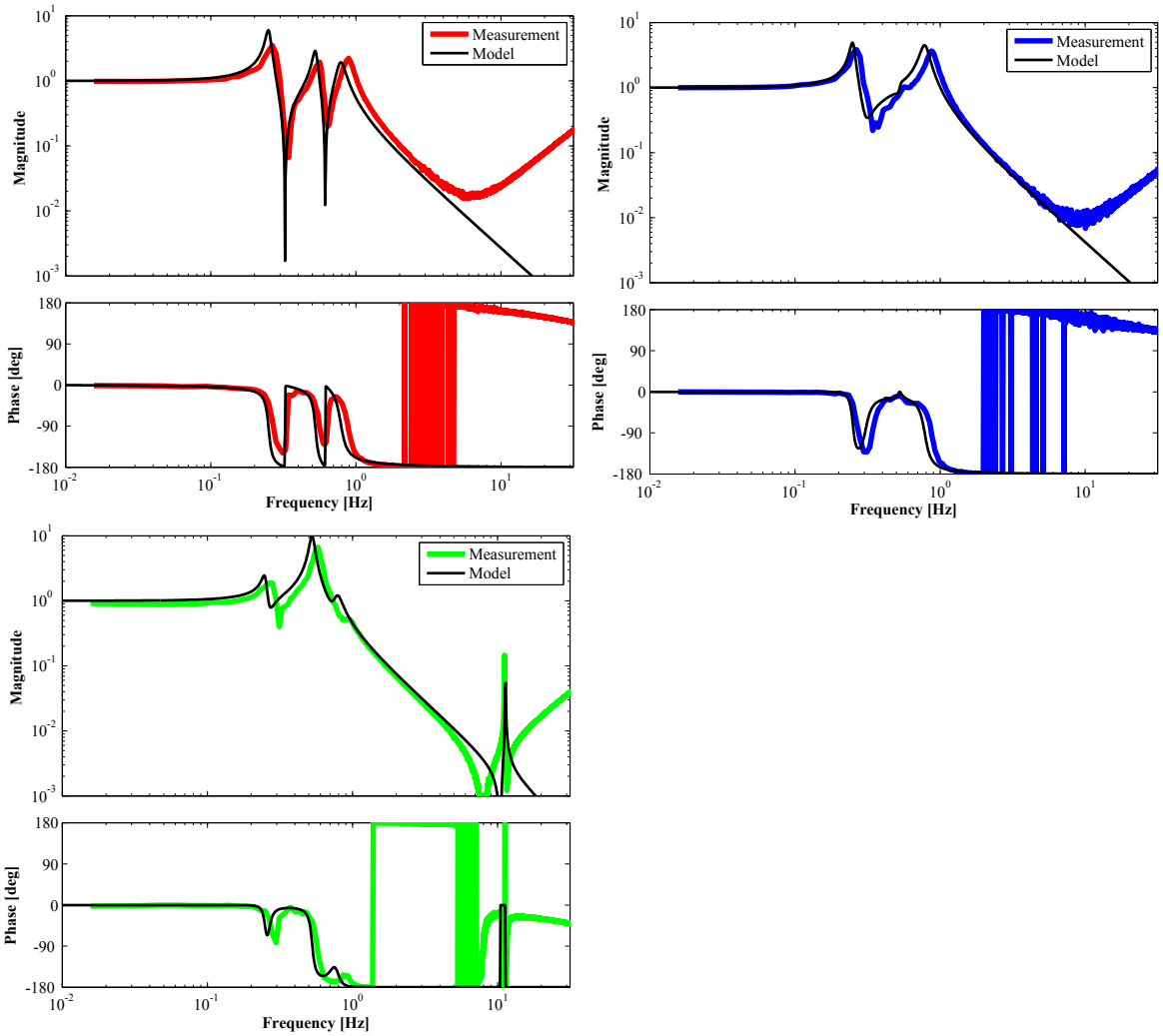

Figure 8.6: Comparison of measured transfer functions about GAS filters and prediction from simulation.

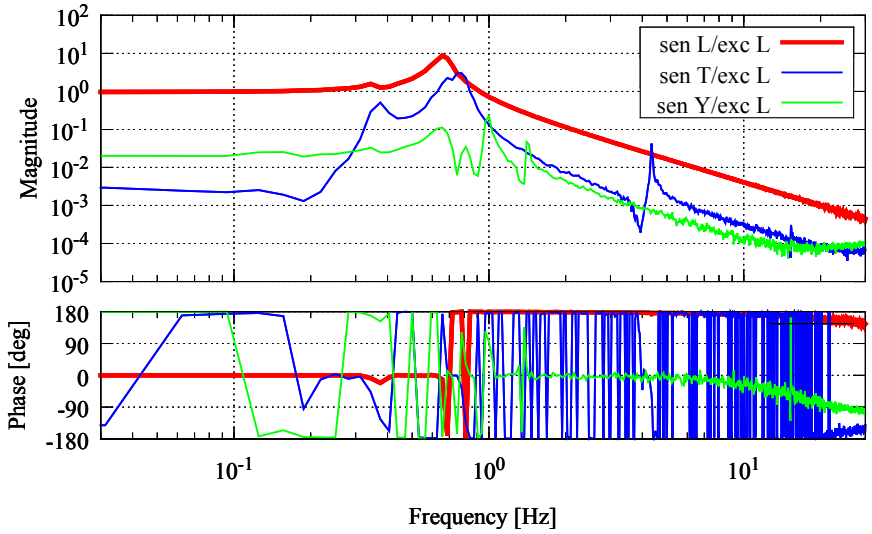

Figure 8.7: Measured transfer functions from the TM-RM longitudinal actuator to the displacements including the coupling with other DoFs.

large couplings at the high frequency. Especially couplings from rotational actuators (R, P and Y) to some DoFs are huge. The couplings to the longitudinal motions could be problematic since they can cause control noise coupling to the interferometer signals. The noise couplings to the TM longitudinal motion are discussed later. The couplings of F0 actuators are also huge at the low frequency, while they are not so large as to affect the control stability.

	sensor L		sensor P		sensor Y	
	10 mHz	10 Hz	10 mHz	10 Hz	10 mHz	10 Hz
actuator L	1		0.003	0.075	0.021	0.035
actuator P	0.005	0.099	1		0.001	0.013
actuator Y	0.005	0.007	0.002	0.011	1	

Table 8.1: Coupling conefficeints in the TM stage

8.2.7 Summary of this work

Frequency response of the suspension system is investigated by using implemented sensors and actautors. The measured freqency response shows similar tendency as predicted frequency response in the rigid-body model simulation, which proves that mechanical system is working almost as is designed. The differences between the model and actual system are discussed and we have the following findings:

	sensor L	sensor T	sensor V	sensor R	sensor P	sensor Y
actuator L	1	0.001	0.002	0.002	0.011	0.001
actuator T	0.000	1	0.000	0.001	0.002	0.010
actuator V	0.003	0.001	1	0.010	0.004	0.002
actuator R	0.001	0.001	0.001	1	0.002	0.002
actuator P	0.005	0.003	0.011	0.023	1	0.010
actuator Y	0.000	0.007	0.004	0.003	0.000	1

Table 8.2: Coupling conefficeints in the IM stage at 10 mHz

	sensor L	sensor T	sensor V	sensor R	sensor P	sensor Y
actuator L	1	0.001	0.007	0.011	0.001	0.027
actuator T	0.006	1	0.006	0.009	0.013	0.015
actuator V	0.027	0.003	1	0.032	0.018	0.011
actuator R	0.165	0.627	0.019	1	0.417	0.030
actuator P	0.267	0.008	0.025	0.017	1	0.023
actuator Y	0.113	0.622	0.035	0.018	0.034	1

Table 8.3: Coupling conefficeints in the IM stage at 10 Hz

	sensor L		sensor T		sensor Y	
	10 mHz	10 Hz	10 mHz	10 Hz	10 mHz	10 Hz
actuator L	1		0.874	0.012	0.389	0.010
actuator T	0.253	0.014	1		0.466	0.016
actuator Y	0.263	0.086	0.739	0.031	1	

Table 8.4: Coupling conefficeints in the F0 stage

- Electro-magnetic couplings of sensor signals with actuation signals change the shape of transfer functions in the high frequency regime.
- The resonant frequencies regarding the RM suspension deviate from simulated values, probably due to a floating wire in a bad hunging condition.
- Large couplings in transfer functios about F0 indicate asymmetry of the IP stiffness.
- Actuator diagonalzation works well for IM and TM actuators. However it does not reduce the couplings between different DoFs at high frequencies, which might cause large control noise coupling to the interferometer signals.

8.3 Performance of damping controls

Here active damping servos are switched on and the decay time reduction of mechanical resonances is confirmed. The servo filters are designed based on the frequency responses from actuators to sensors mentioned above. Since measured frequency responses deviate from simulated responses due to non-mechanical couplings at higher frequencies, we need to reduce the control gains at these frequencies with low-pass filters in suitable cut-off frequencies. The decay time of mechanical resonances in the passive system is investigated and compared with that in the actively-controlled system.

8.3.1 Control servos

The damping control loops are built in the TM, IM and F0 levels using OSEMs or LVDT-actuator units. Resonances about vertical GAS filter modes are damped by an LVDT-actuator unit in the top GAS filter (F0).

To achieve viscous damping of mechanical resonances, one has to apply actuation force proportional to the velocity of the target. Since shadow sensors in OSEMs and LVDTs are displacement sensors, the signals have to be converted to velocities by applying differntiation filters and sent to actuators with multiplying appropriate gain. Therefore feedback filters should have gain proportional to f around the frequencies of resonances to be damped. However, an ideal differentiation filter has an infinite gain at $f \to \infty$ and is not applicable in actual feedback filters. Therefore we need to roll off the control gain by adding a low-pass filter with a certain cut-off frequency. The cut-off frequencies are set lower than the frequencies where the electro-magnetic couplings of sensors and actuators become dominant. The typical frequencies are 50 Hz for OSEMs and 5 Hz for LVDT-actuator units. The cut-off frequencies are set even lower in some DoFs to avoid exciting mechanical resonances around these frequencies.

The following figures show bode plots of designed servo filters. For the F0 and GAS controls, the control gains are raised at low frequencies for thermal drift compensation. The gains of damping controls are tuned to acquire optmial damping strength. A resonant

gain introduced around 0.16 Hz to the IM yaw control is required to damp the torsion mode of the IM suspension wire sufficiently.

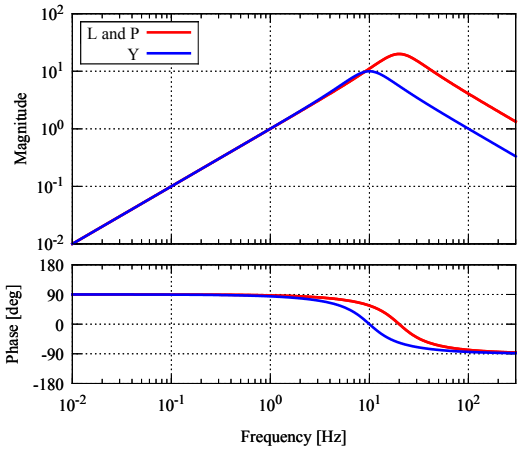

Figure 8.8: TM control servo filters.

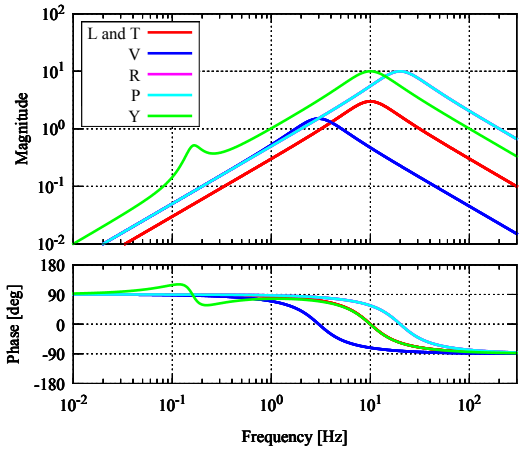

Figure 8.9: IM control servo filters.

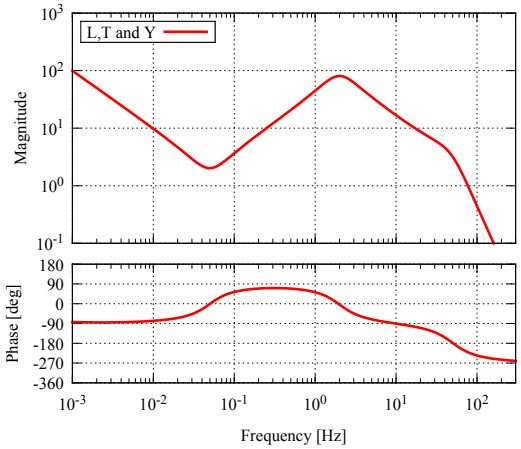

Figure 8.10: F0 control servo filters.

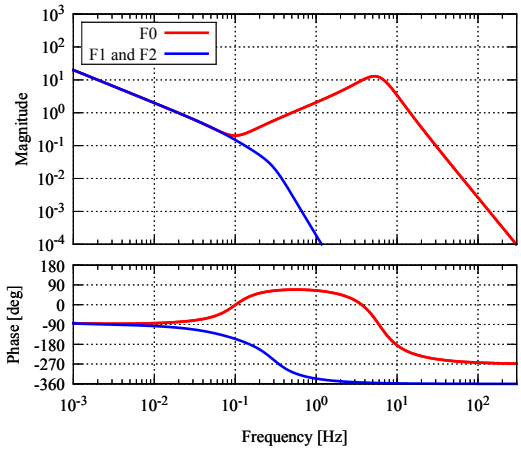

Figure 8.11: GAS control servo filters.

8.3.2 Stability check

In order to check the stablity of the controls, the open loop gains of each control loop is measured. Fig. **??** shows the signal flows of the measurement in the system under active controls. Random noise is injected to the virtual actuator about a certain DoF, and resulting feedback signals are monitored. The open loop gain is calculated as $G(\omega) = \tilde{s}/\tilde{a}$.

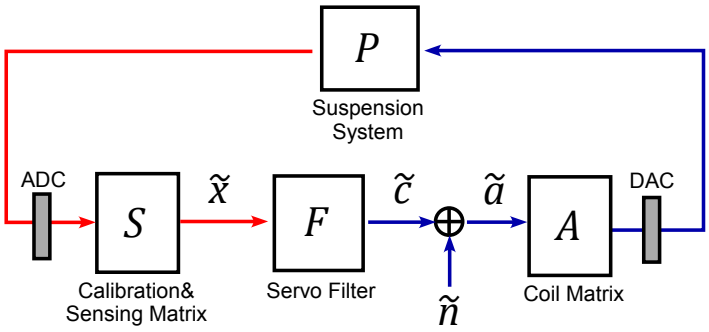

Figure 8.12: Signal flows in the open loop gain measurement.

8.3.3 Decay time of mechanical resonances

In order to check if the mechanical resonances are properly damped by the active controls, we survey mechanical resonances of the suspension system and check the decay time before and after controls are switched on. Decay time of a mechanical resonance is taken by exciting the system with an appropriate actuator and measuring decay signal from implemented vibration sensors. The decay signals are fit with a sine wave with exponential decay:

$$f(t) = A \exp(-t/\tau) \sin(2\pi f_0 t + \varphi) + B. \tag{8.1}$$

The time constant τ indicates the $1/e$ decay time of the mechanical resonance. Sometimes it is difficult to excite only one resonant mode and we obtain a superposition of two sine waves. This can happen when there exist mechanical resonaces with close eigen frequencies. In such a case, we fit the signals by sum of two decay sine waves.

Table 8.5 shows a list of mechanical resonances of the suspension system predicted in a rigid-body model simulation. It only shows the mechanical reosnances with eigen frequencies less than 20 Hz.

Table 8.6 and 8.7 shows measured resonant frequencies and decay time of resonant modes.

No.	Frequency [Hz]	Mode Shape	Note
#1	0.0505	YF1, YF2, YIR, YIM, YRM, YTM	wire torsion
#2	0.0794	LF0, LMD, LF1, LF2, LIR, LIM, LRM, LTM	IP translation
#3	0.0794	TF0, TMD, TF1, TF2, TIR, TIM, TRM, TTM	IP translation
#4	0.1232	-YF0, YIM, YRM, YTM	IP rotation
#5	0.1390	-YF1, YIM, YRM, YTM	wire torsion
#6	0.1616	-YF2, -YIR, YIM, YRM, YTM	wire torsion
#7	0.2494	VF2, VIR, VIM, VRM, VTM	GAS filter
#8	0.3021	RIM, RRM, RTM	IM roll
#9	0.3418	PIM, PRM, PTM	IM pitch
#10	0.4094	TIM, TRM, TTM, RTM	main pendulum
#11	0.4196	LIM, LRM, LTM, PTM	main pendulum
#12	0.5247	-VF1, -VF2, -VIR, VIM, VRM, VTM	GAS filter
#13	0.5468	TMD	MD pendulum
#14	0.5470	LMD	MD pendulum
#15	0.5502	YMD	MD yaw
#16	0.5740	RF2, RIR	F2 roll
#17	0.5787	PF2, PIR	F2 pitch
#18	0.5889	RF1	F1 roll
#19	0.6331	-PF1, LTM, -PTM	main pendulum
#20	0.6485	RF1, TTM, RTM	main pendulum
#21	0.6571	-LRM, LTM, -PTM	TM-RM pendulum
#22	0.6580	TRM, TTM, RTM	TM-RM pendulum
#23	0.6863	PF1	F1 pitch
#24	0.7923	VF1, -VF2, -VIR	GAS filter
#25	0.8162	PTM	TM pitch
#26	1.0009	-YIM, -YRM, YTM	TM yaw
#27	1.0325	YIR	IR yaw
#28	1.1844	TIM, -TTM, -TRM	IM pendulum
#29	1.1851	LIM, -LIM, -LRM	IM pendulum
#30	1.2101	RF2, -TIR, RIR	F2 roll
#31	1.2134	PF2, LIR, PIR	F2 pitch
#32	1.3798	-YIM, YRM, YTM	RM yaw
#33	1.4738	TIR	IR pendulum
#34	1.4759	LIR	IR pendulum
#35	4.8559	-PIM, PRM	RM pitch
#36	11.320	VTM	TM vertical
#37	15.528	RTM	TM roll

Table 8.5: Eigen mode list predicted in a rigid-body model simulation.

	Frequency [Hz]					
No.	measured	simulated	difference [%]	τ [sec]	Q factor	exc. point
#1	0.061	0.0505	20.7	56	11	YF0
#2/#3	0.081	0.0794	2.5	30	8	LF0
#4	0.149	0.1232	20.9	6	3	YF0
#5	0.150	0.1390	7.7	50	24	YF0
#6	0.172	0.1616	6.2	13	7	YF0
#7	0.263	0.2494	5.6	15	13	VF0
#8	0.297	0.3021	1.9	138	129	RIM
#9	0.371	0.3418	8.4	170	198	PIM
#10	0.405	0.4094	1.0	10	12	TF0
#11	0.424	0.4196	1.0	13	17	LF0
#12	0.539	0.5247	2.7	6	9	VF0
#13	-	0.5468	-	-	-	-
#14	-	0.5470	-	-	-	-
#15	-	0.5502	-	-	-	-
#16	0.545	0.5740	0.6	71	122	TIM
#17	0.543	0.5787	0.6	79	135	LIM
#18	-	0.5889	-	-	-	-
#19/#20	0.639	0.6331	1.1	77	154	LF0
#21	0.659	0.6571	0.7	1448	2996	LTM
#22	0.655	0.6580	0.4	442	909	TF0
#23	-	0.6863	-	-	-	-
#24	0.861	0.7923	8.7	4	10	VF0
#25	0.793	0.8162	2.9	274	683	PTM
#26	1.000	1.0009	0.1	1295	4069	YTM
#27	1.020	1.0325	1.2	268	857	YIM
#28/#30	1.169	1.2101	3.4	101	371	TIM
#29/#31	1.178	1.2134	2.9	37	135	LIM
#32	1.406	1.3798	1.9	782	3456	YTM
#33/#34	1.456	1.4728	1.0	32	143	TF0
#35	4.361	4.8559	10.2	9	119	PTM
#36	11.11	11.320	1.9	7	237	VIM
#37	15.25	15.528	1.8	5	235	RIM

Table 8.6: Measured resonant frequencies and decay time without control.

	Frequency [Hz]					
No.	damped	undamped	difference [%]	τ [sec]	Q factor	exc. point
#1	0.065	0.061	5.6	43	8.6	YF0
#2/#3	0.149	0.081	45.6	2.8	1.3	LF0
#4/#5	0.147	0.15	1.9	11	5.2	YF0
#6	0.159	0.172	8.4	25	13	YF0
#7	0.288	0.263	8.5	6.6	6.6	VF0
#8	0.296	0.297	0.3	4.7	4.4	RIM
#9	0.380	0.371	0.3	4.6	5.6	PIM
#10	0.384	0.405	5.2	3.7	4.4	TF0
#11	0.405	0.424	4.5	2.8	3.5	LF0
#12	0.592	0.539	8.9	3.8	7.0	VF0
#13	-	-	-	-	-	-
#14	-	-	-	-	-	-
#15	-	-	-	-	-	-
#16	0.547	0.545	0.7	0.33	0.6	TIM
#17	0.549	0.543	0.7	5.1	8.7	LIM
#18	-	-	-	-	-	-
#19/#20	0.627	0.639	1.8	6.5	13.0	LF0
#21	0.694	0.659	5.0	0.85	1.9	LTM
#22	0.655	0.655	0.0	165	339	TF0
#23	-	-	-	-	-	-
#24	-	0.861	-	-	-	-
#25	0.826	0.793	4.0	0.45	1.2	PTM
#26	0.969	1.000	3.2	0.24	0.7	YTM
#27	1.006	1.020	1.4	8.1	26	YIM
#28/#30	1.180	1.176	0.3	32.5	120	TF0
#29/#31	1.180	1.176	0.3	22.5	84	LF0
#32	1.324	1.406	6.2	2.91	12	YTM
#33/#34	1.446	1.445	0.1	24.8	113	TF0
#35	4.383	4.361	0.5	1.9	26	PTM
#36	11.11	11.11	0.0	6.8	237	VIM
#37	15.30	15.25	0.3	13.6	654	RIM

Table 8.7: Measured resonant frequencies and decay time with control.

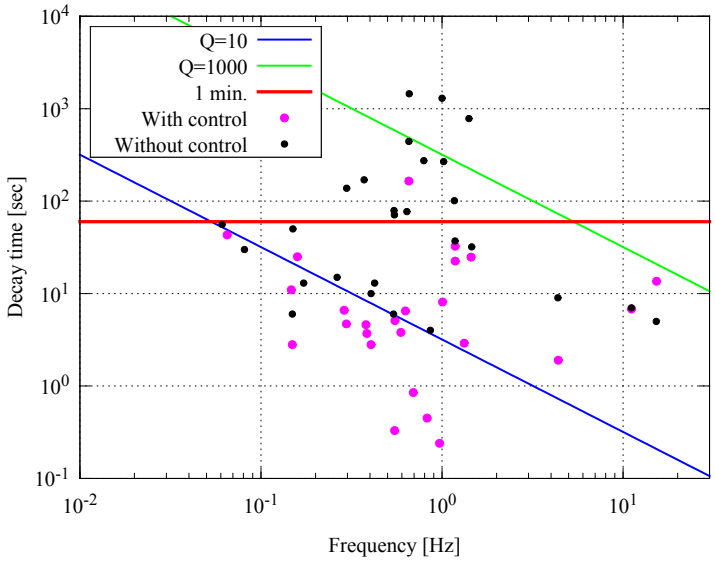

Figure 8.13: Decay time versus resonant frequency plot.

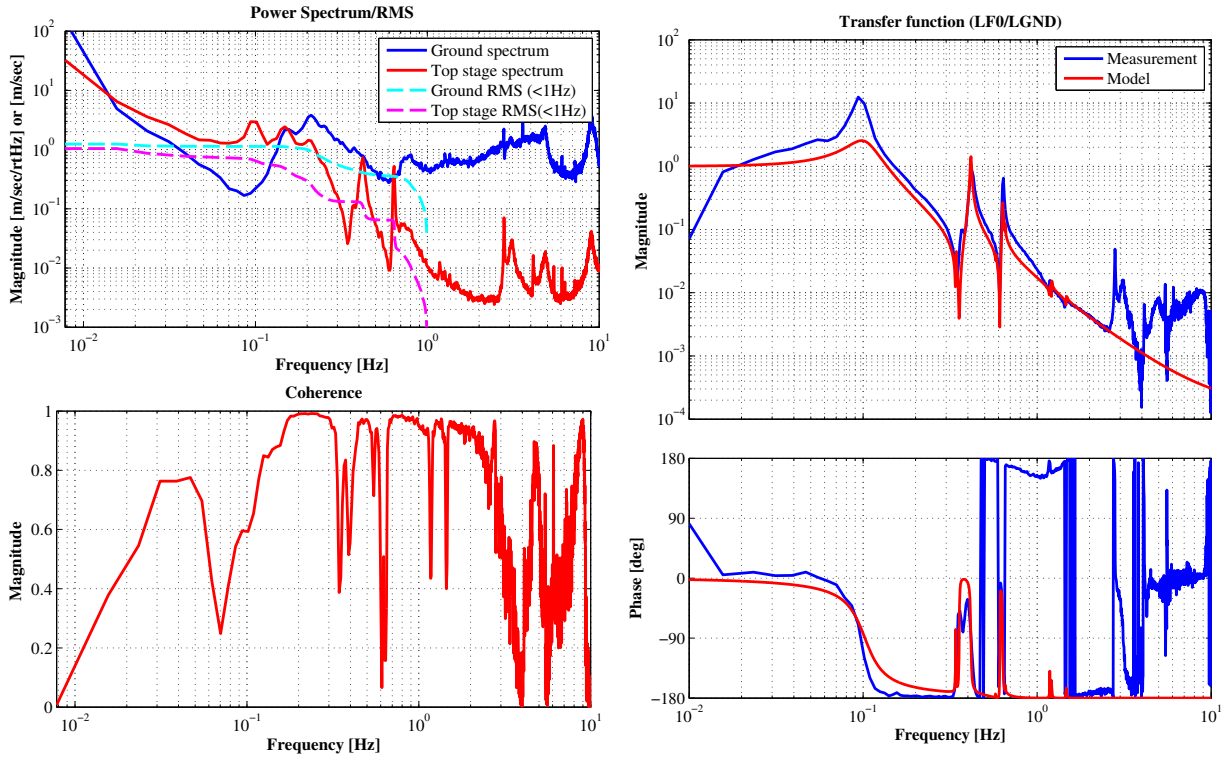

Figure 8.14: IP transfer function measurement without control

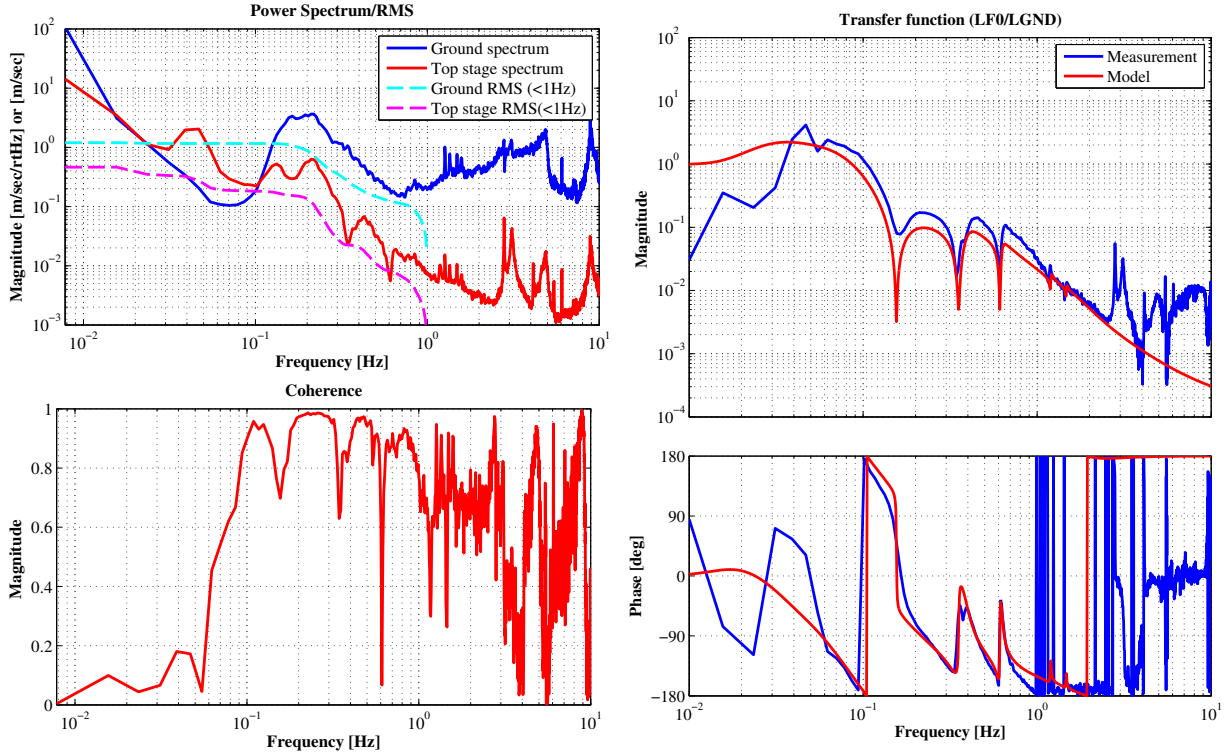

Figure 8.15: IP transfer function measurement with control

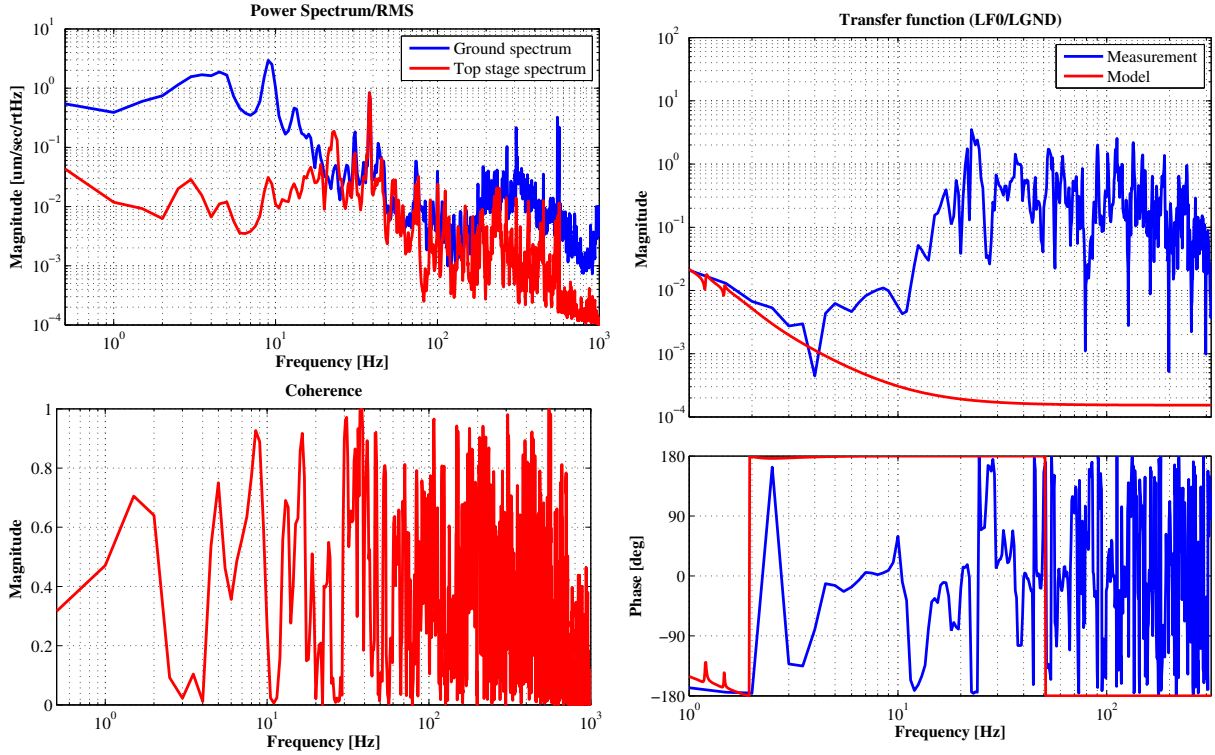

Figure 8.16: IP transfer function measurement high frequency

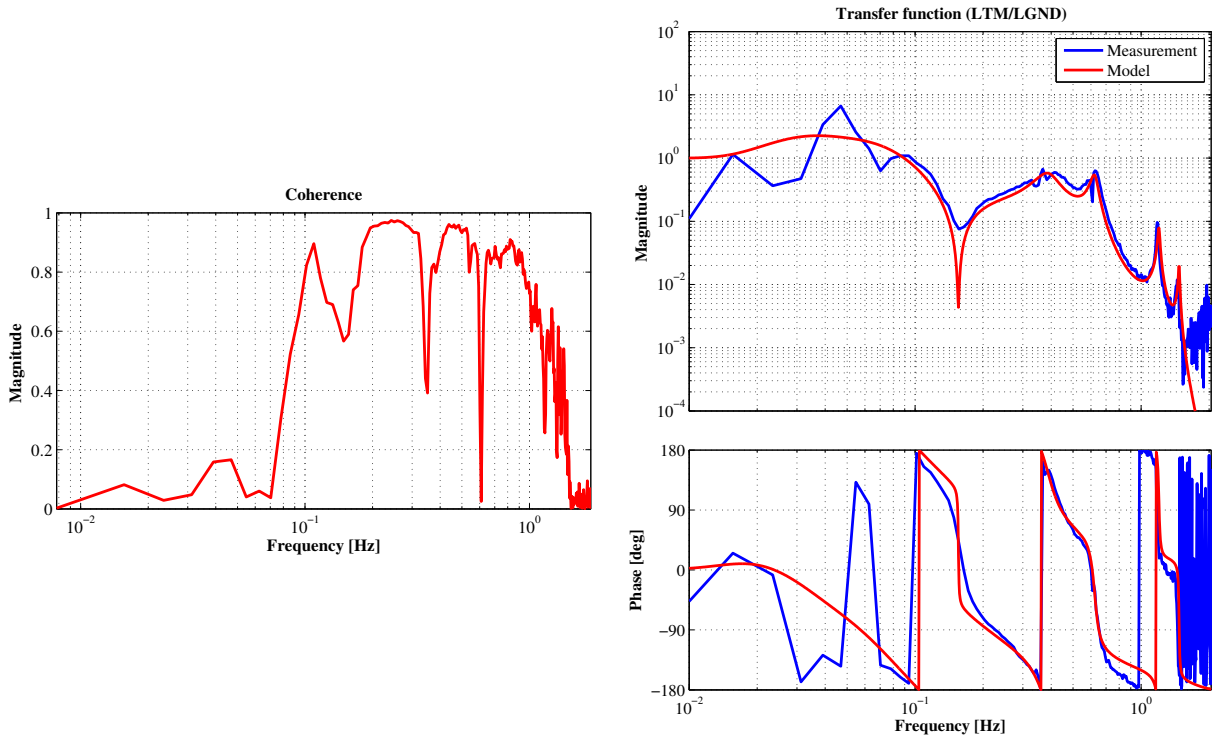

Figure 8.17: Transfer function from ground to TM.

8.4 Performance of inverted pendulum

8.4.1 Vibration transferred to the top stage

8.4.2 Vibration transferred to the test mass

8.5 Control using optical lever

We introduce angular control of the TM using optical lever signals fed back to the actuators on IM.

8.5.1 Transfer functions from actuators to optical lever signals

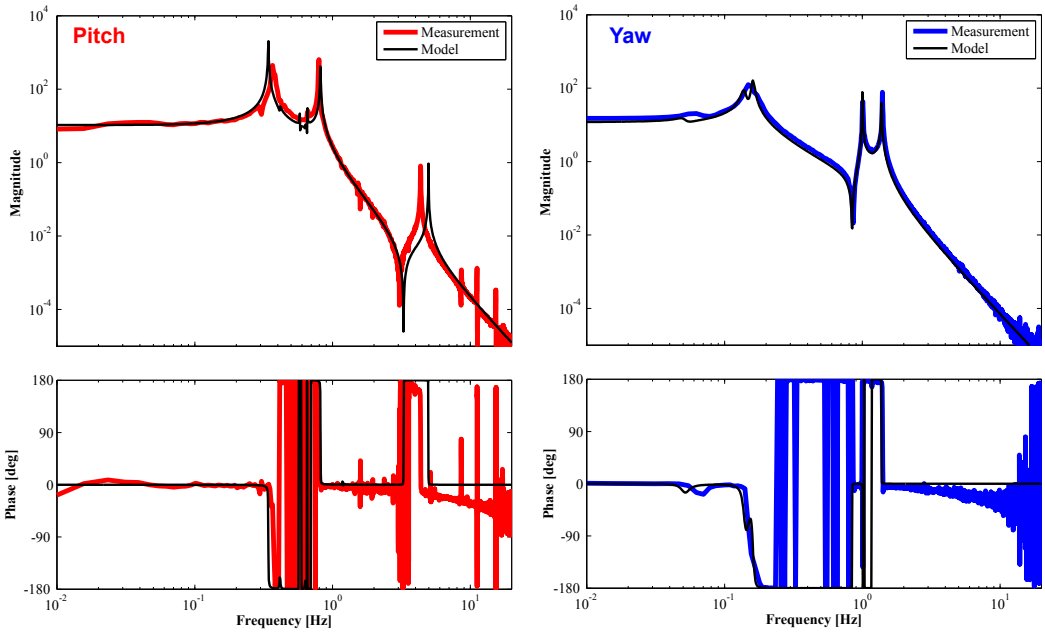

Figure 8.18: Transfer function from actuators to optical levers

8.5.2 Control servos

8.5.3 Performance

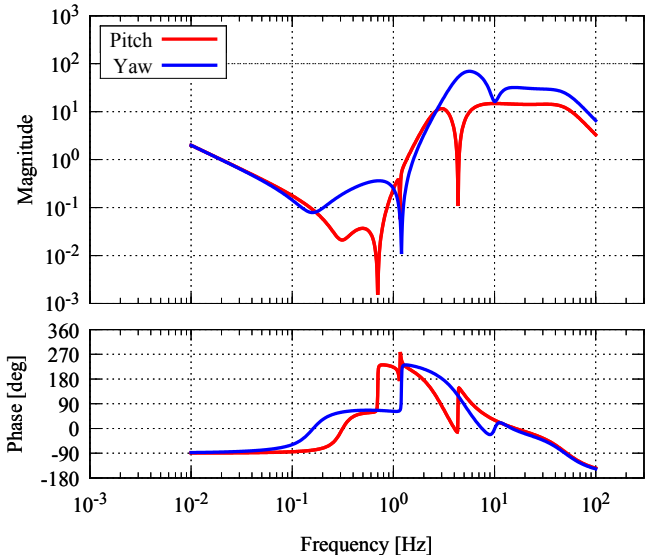

Figure 8.19: Servo filter design.

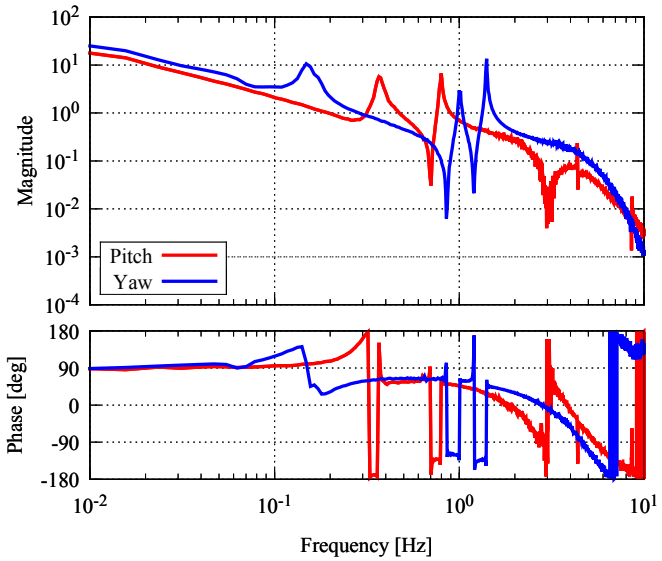

Figure 8.20: Open loop transfer functions.

Design study on KAGRA type-A SAS

Chapter 9

9.1 Theory and background

Summary and futre works

Chapter 10